

Secondary organic aerosol production from local emissions dominates the organic aerosol budget over Seoul, South Korea, during KORUS-AQ

Benjamin A. Nault, Pedro Campuzano-Jost, Douglas A. Day, Jason C. Schroder, Bruce Anderson, Andreas J. Beyersdorf, Donald R. Blake, William H. Brune, Yonghoon Choi, Chelsea A. Corr, Joost A. de Gouw, Jack Dibb, Joshua P. DiGangi, Glenn S. Diskin, Alan Fried, L. Gregory Huey, Michelle J. Kim, Christoph Knote, Kara D. Lamb, Taehyoung Lee, Taehyun Park, Sally E. Pusede, Eric Scheuer, Kenneth L. Thornhill, Jung-Hun Woo, Jose L. Jimenez

Angaben zur Veröffentlichung / Publication details:

Nault, Benjamin A., Pedro Campuzano-Jost, Douglas A. Day, Jason C. Schroder, Bruce Anderson, Andreas J. Beyersdorf, Donald R. Blake, et al. 2018. "Secondary organic aerosol production from local emissions dominates the organic aerosol budget over Seoul, South Korea, during KORUS-AQ." *Atmospheric Chemistry and Physics* 18 (24): 17769–800.
<https://doi.org/10.5194/acp-18-17769-2018>.



Supplement of

Secondary organic aerosol production from local emissions dominates the organic aerosol budget over Seoul, South Korea, during KORUS-AQ

Benjamin A. Nault et al.

Correspondence to: Jose L. Jimenez (jose.jimenez@colorado.edu)

The copyright of individual parts of the supplement might differ from the CC BY 4.0 License.

S1. KORUS-AQ Overview

Table S1. List of NASA DC-8 research flights and date of take-off. Unless noted, the take-off dates are different than the local dates since the data was recorded in UTC. We document the research flights with the UTC dates to correspond with the data repository (Aknan and Chen, 2018).

<i>Research Flight Number</i>	<i>Date of Take-off</i>	<i>Regions Sampled</i>	<i>Number of Seoul Missed Approaches</i>
01	01/May/2016	Jeju jetway (×2)	3
02	03/May/2016	Yellow Sea, Jeju jetway	3
03	04/May/2016	Jeju jetway	2
04	06/May/2016	Busan jetway (×2)	3
05	10/May/2016	Jeju jetway, other ^b	2
06	11/May/2016	Yellow Sea, other ^c	3
07	12/May/2016	Yellow Sea, other ^d	0
08	16/May/2016	Jeju jetway, Busan jetway	3
09	17/May/2016	Yellow Sea, Busan jetway	3
10	19/May/2016	Busan jetway (×2)	3
11	21/May/2016	Yellow Sea	3
12	24/May/2016	Yellow Sea	2
13	26/May/2016 ^a	Jeju Jetway	2
14	29/May/2016	Yellow Sea, Busan jetway	4
15	30/May/2016	Yellow Sea, Jeju jetway	3
16	01/June/2016	Busan jetway, Jeju jetway	3
17	02/June/2016	Busan jetway, Jeju jetway	3
18	04/June/2016	Yellow Sea, other ^e	5
19	08/June/2016	Busan jetway (×2)	3
20	09/June/2016	Jeju jetway, other ^b	2

^aFor RF13, the DC-8 took-off after 00:00 UTC, corresponding to the date in local time and UTC time being the same.

^bThe DC-8 sampled south of the Korean peninsula.

^cThe DC-8 sampled east of Seoul to the Sea of Japan.

^dThe DC-8 sampled the Sea of Japan.

^eThe DC-8 remained in the greater Seoul area to sample point sources.

Table S2. Description of the geographical locations used in Figure 1 and throughout the text, and shown in Figure S1..

<i>Location</i>	<i>Lat Min (°N)</i>	<i>Lat Max (°N)</i>	<i>Lon Min (°E)</i>	<i>Lon Max (°E)</i>
Seoul	36.8	37.6	124.6 ^a	128.0
Yellow Sea			124.0	126.0
Jeju jetway	34.2	36.8	126	127
Busan jetway	35.2	36.8	128.6	129.9

^aThis value was chosen to include the Seoul outflow observed during RF11 and RF18.

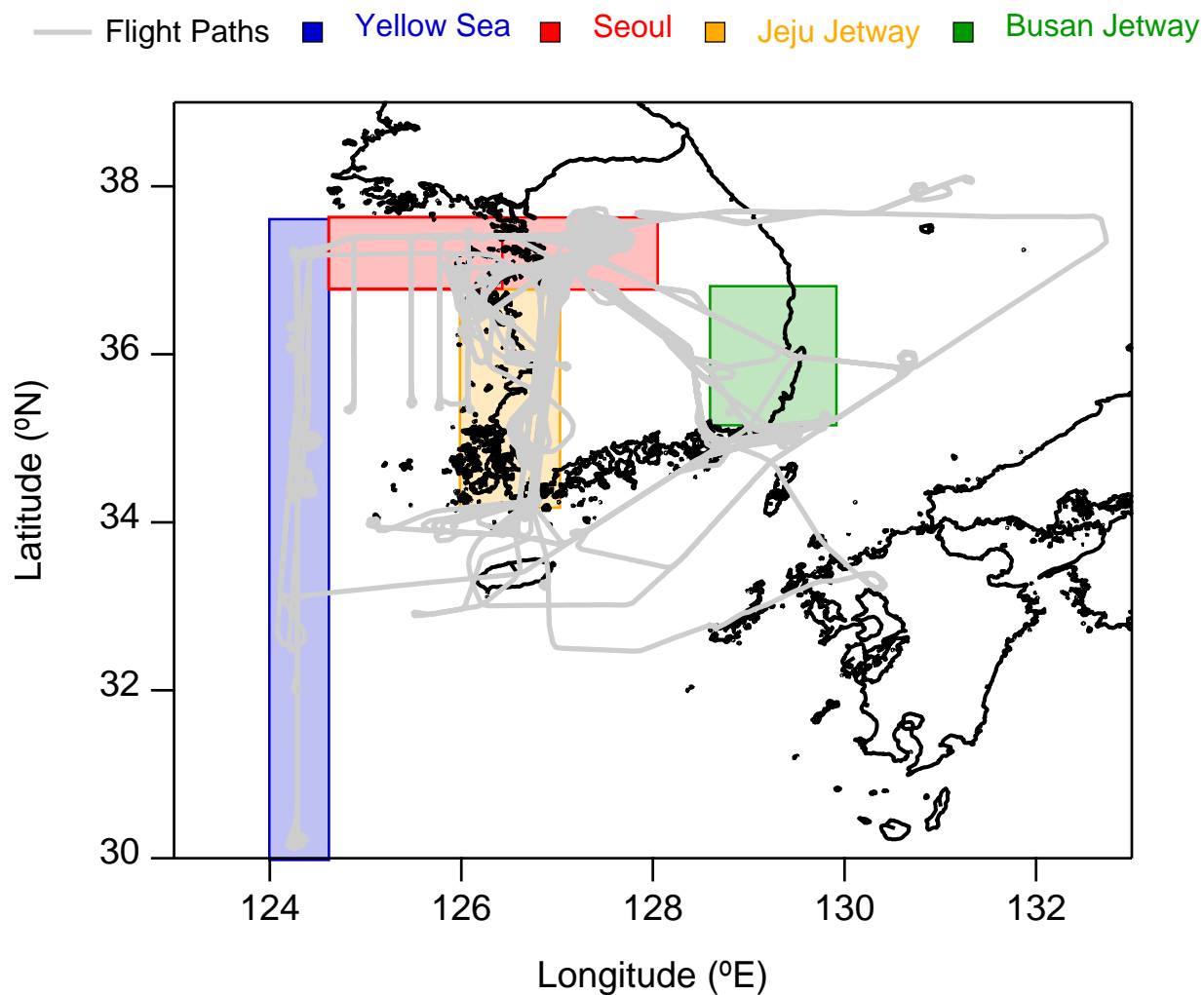


Figure S1. Geographical regions shown in SI Table 1. Note, the Seoul box is extended into the Yellow Sea to capture the outflow of Seoul emissions for two flights (RF11 and RF18).

S2. CU-AMS Sampling and Calibration

After almost every flight, the ionization efficiency (IE) was calibrated (Figure S3) using the single particle technique. Briefly, air containing 150 – 250 particles/cm³ of NH₄NO₃, of 400 nm (mobility diameter, sized with a differential mobility analyzer, TSI model 3080, that was installed in the same rack as the CU-AMS) was sampled by the AMS. Thresholds of 4 (*m/z* 30) or 3 (*m/z* 46) ions per event were selected to produce a low, but detectable background (typically ~7 events/cm³ background). An event would be recorded, after evaporation and ionization of NH₄NO₃ particle, if at least 4 (*m/z* 30) or 3 (*m/z* 46) ions were observed. These values were analyzed using the ToF AMS Ionization Efficiency Calibration Panel for ET, v1.0.5F (http://cires1.colorado.edu/jimenez-group/ToFAMSResources/ToFSoftware/index.html#ToF_IE_Cal), to process the data and calculate IE and IE/AB (AB is air beam). Typical values during KORUS-AQ, for 400 nm (mobility diameter) NH₄NO₃ calibrations were the following: 10 baseline segments and minimum and maximum ions per particle values of 1 and 200. During KORUS-AQ, the average IE/AB was $8.10(\pm 0.64) \times 10^{-13}$ ions/molecule of nitrate, which leads to an overall 10% variability for this value during the whole campaign. Further details about using single particle technique for IE/AB calibrations can be found in Nault et al. (2016).

These IE calibrations also provided relative ionization efficiency (RIE) calibrations of NH₄ after nearly every flight, as well (Figure S3), along with the NO⁺ and NO₂⁺ ratios of ammonium nitrate, which are useful to estimate particle organic nitrate concentrations, as detailed in Fry et al. (2013). The SO₄ and Chl RIEs were measured about once every week, and the interpolated values were used for the SO₄ and Chl concentrations. For the organic aerosol, we used an RIE of 1.4 (Jimenez et al., 2016; Xu et al., 2018). Finally, to test the effects of solution mixtures on RIE for

SO₄ and NH₄, we made calibration solutions ranging from 0 – 100% NH₄NO₃, with the balance coming from (NH₄)₂SO₄. We find no effects, both on the calculated NH₄ balance (Figure S6), when using the NH₄ and SO₄ RIE's from the pure calibration, and on the recalculated NH₄ (SO₄) RIE when keeping a constant SO₄ (NH₄) RIE from the pure calibrations (Figure S6). The consistency in the NH₄ balance, as observed in prior studies (Docherty et al., 2011; Jimenez et al., 2016), and the high precision (3% precision in all calculations) provides further confidence in the stability of the RIEs for the species in calculating their mass in mixed particles, and indicates that there are no effects on the RIE with changing composition, and, thus, CE (Jimenez et al., 2016).

Also, the IE calibrations performed after each flight provided an opportunity to calculate the effect of pNO₃ on producing a small artifact CO₂⁺ signal, as detailed in Pieber et al. (2016), and of pNO₃ on producing small artifact HCl⁺ and Cl⁺ signal, as detailed in Hu et al. (2017a) (Figure S3). The CU-AMS data has been corrected for these small effects. The corrections were typically 1% of CO₂⁺ and 0.8% Chl.

Three different lens transmission calibrations to characterize the high end of the AMS transmission curve were performed: (1) comparing the NH₄NO₃ mass measured with the CPC and the CU-AMS between 200 – 450 nm (mobility diameter, d_m); (2) comparing the number of particles measured with the CPC and the CU-AMS between 300 – 450 nm (d_m) using the single particle vaporization technique detailed above; and (3) comparing the (NH₄)₂SO₄ mass measured with the CPC and the CU-AMS between 250 – 450 nm (d_m), normalizing to the value at 250 nm. The NH₄NO₃ diameters were converted to vacuum aerodynamic diameters (d_{va}), as discussed in DeCarlo et al. (2004). As seen in Figure S4, both techniques show good agreement for the particle transmission, and this transmission is similar to the recommended transmission curve in the literature (Knote et al., 2011; Hu et al., 2017b). For this curve, it is assumed that the transmission

linearly increases from 0 – 100% between 40 – 100 nm (d_{va}) (Zhang et al., 2004), remains 100% between 100 – 550 nm (aerodynamic diameter), and decreases linearly from 100 – 0% between 550 nm – 1500 nm (d_{va}). This leads to a 50% cut-off of ~900 nm (d_{va}) during KORUS-AQ.

The particle sizing in the AMS Particle Time-of-Flight (PToF) mode was calibrated with PSLs, ranging from 70 – 700 nm (geometric diameter) (Figure S5). This calibration was compared against the velocities calculated from data collected during the NH_4NO_3 lens transmission measurements. As seen in Figure S5, these two different methods to calibrate the PToF velocity show comparable results, falling within the 95% confidence interval of the PSL calibration. The fact that both PToF calibrations agree, and that the SMPS used for the AN calibrations showed less than 2 nm deviation from the nominal PSLs diameters at all sizes increases our confidence in accuracy of the IE calibration described above, and in particular on lack of evaporation of NH_4NO_3 after its size selection in the DMA.

Finally, the vaporizer power, and thus, temperature, was calibrated by using monodisperse NaNO_3 particles of $d_m = 350$ nm (Figure S8), as recommended by Williams (2010) and Hu et al. (2017b). This method is more accurate than relying on the temperature reported by the thermocouple on the AMS vaporizer, which can often be unreliable (Williams, 2010; Hu et al., 2017b). The general idea is to increase the vaporizer power between ~1 – 7 W and locate where the NaNO_3 full-width half maximum nearly remains constant, indicating that the vaporizer temperature is ~600°C and allowing for maximum peaks in OA, pNO_3 , and SO_4 while minimizing the influence of refractory species (Williams, 2010; Hu et al., 2017b).

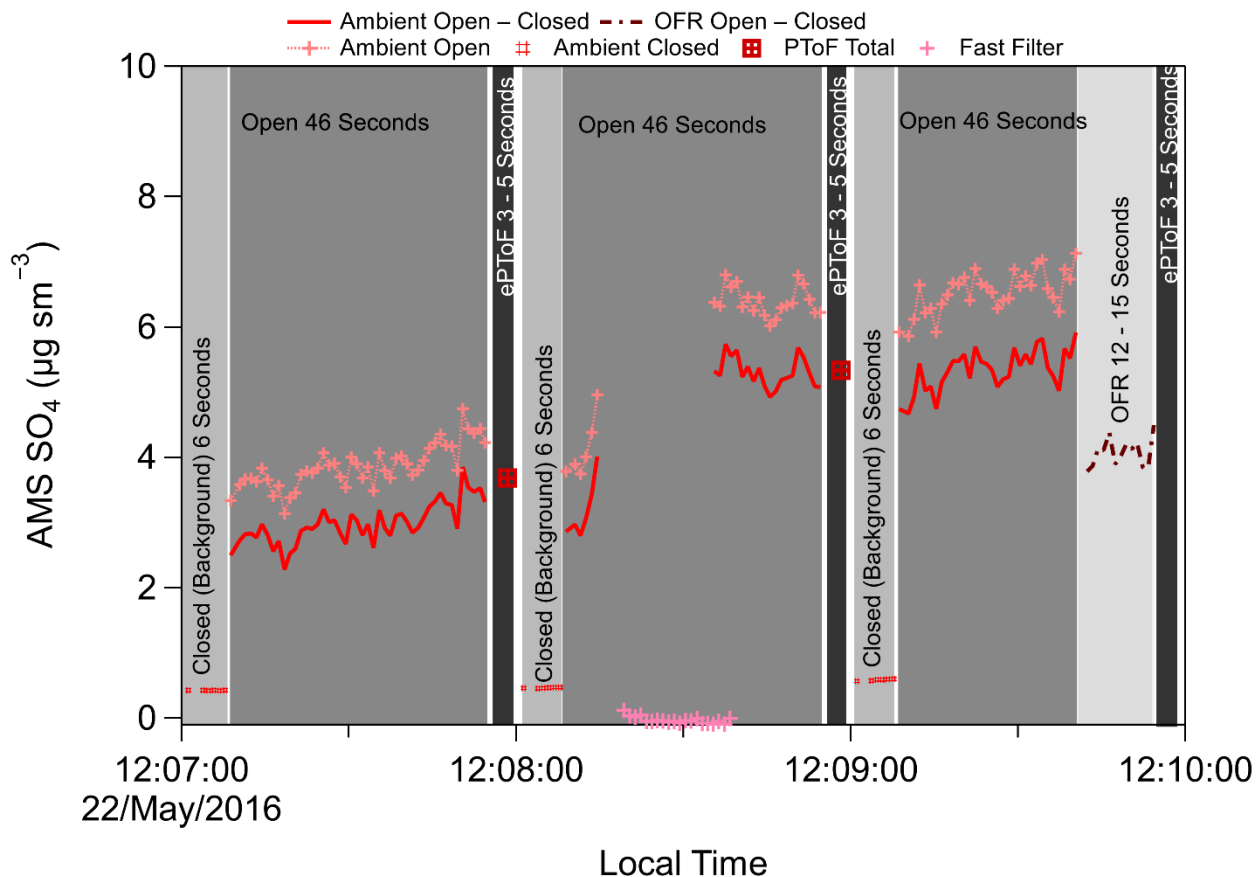
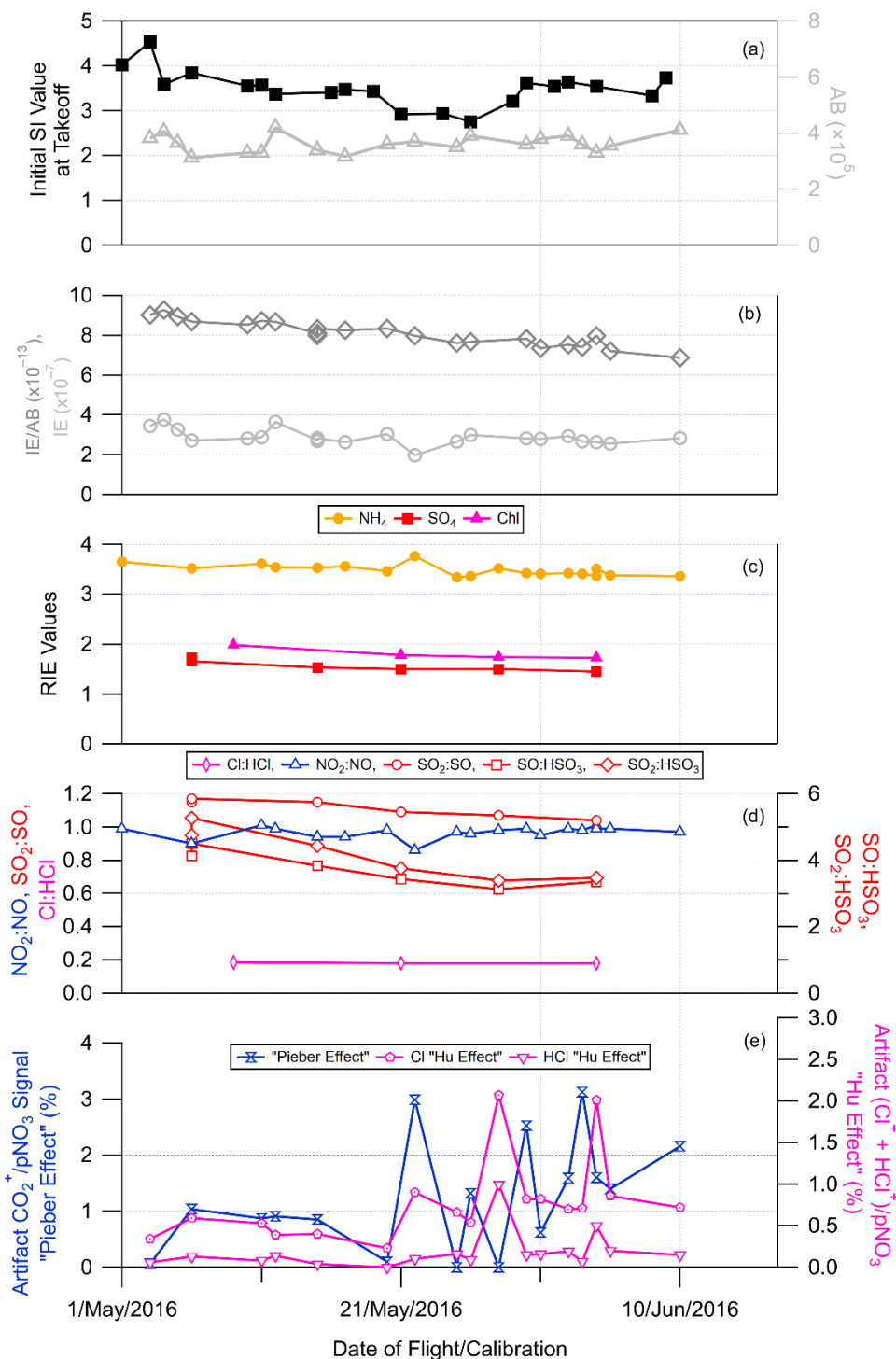


Figure S2. Example time series of the CU-AMS sampling scheme during KORUS-AQ. Though the final 8 s of each minute are dedicated to ePToF, some of the time is used by the computer in saving the 6 s of closed and 46 s of open signal and ePToF signal; therefore, only 3 – 5 s of ePToF signal is actually recorded. The approximate saving time are shown as white spaces.



126

127 **Figure S3.** Time series of the (a) the Single Ion (SI) at take-off for each flight; (b) the air beam
 128 (AB, dark grey), ionization energy (IE, light grey), and IE/AB (middle grey) for each calibration;
 129 (c) the relative ionization energies (RIE) for ammonium (NH_4), sulfate (SO_4), and chloride (Chl)
 130 for each calibration; (d) the ratios of different ions for each calibration; and, (e) measured artifact
 131 signal ratios for $\text{CO}_2^+/\text{pNO}_3$ “Pieber effect” (Pieber et al., 2016) and $(\text{Cl}^+ + \text{HCl}^+)/\text{pNO}_3$ “Hu
 132 effect” (Hu et al., 2017a) effects from each calibration.

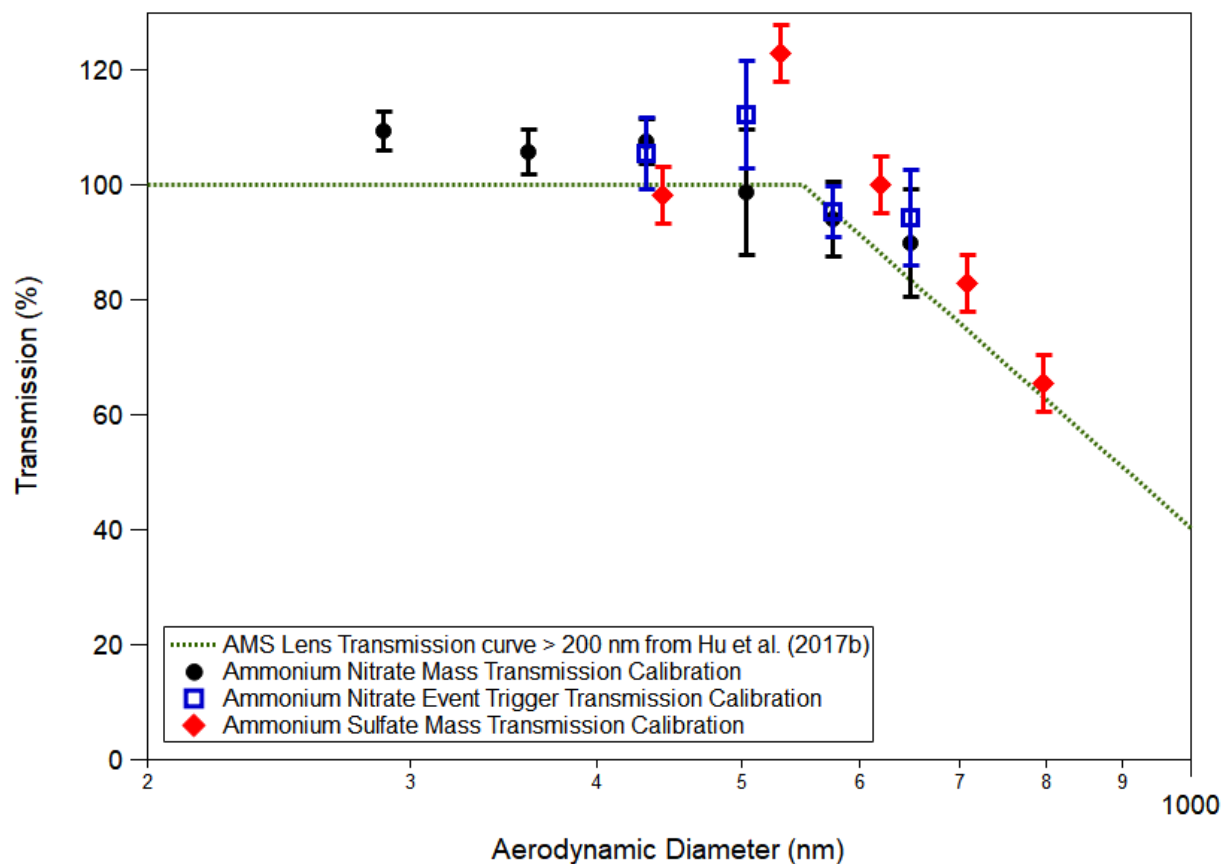


Figure S4. Measured transmission percentage of ammonium nitrate and ammonium sulfate versus vacuum aerodynamic diameters (nm) during KORUS-AQ. The green dashed-line is the expected transmission curve for the CU-AMS from the literature (Knote et al., 2011; Hu et al., 2017b). The black data represents the ammonium nitrate transmission curve using mass closure, from an experiment conducted on 09/May/2016. The blue data represents the ammonium nitrate transmission curve using single particle (“event trigger”) number closure, from an experiment conducted on 17May/2016. The red data represents the ammonium sulfate transmission curve using mass, from an experiment conducted on 06/May/2016. Finally, the error bars represent 1σ variability for the transmission at each size.

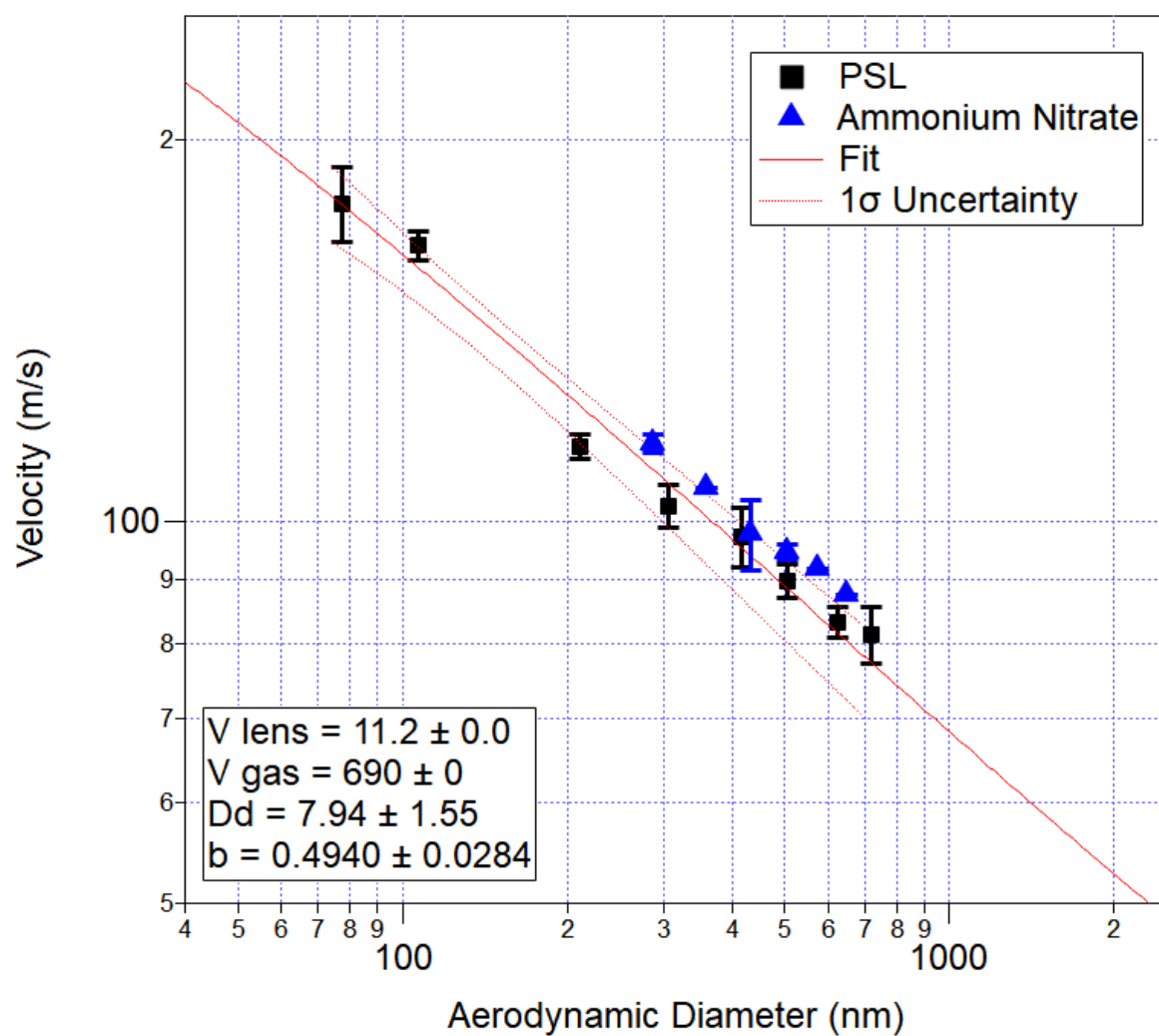
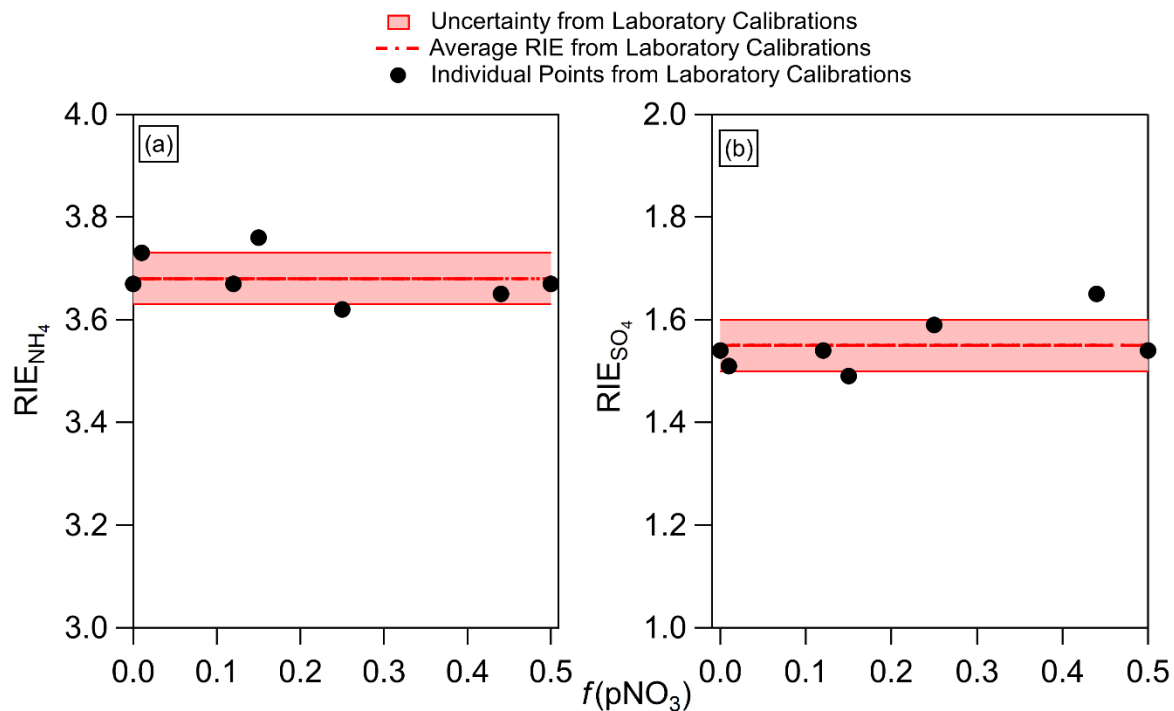


Figure S5. Particle velocity (m/s) inside the AMS vacuum chamber (after exiting the aerodynamic lens) versus vacuum aerodynamic diameter (nm) calibrations for the ePTof mode, using PSLs (black). Solid red line is the fit to the PSLs. The ammonium nitrate measured for the mass closure transmission curves (Figure S4) for comparison to the PSL values.

149

150 **Figure S6.** Ratio of measured and predicted NH_4 from anions versus ratio of nitrate to sulfate
151 mass. Red points are from Docherty et al. (2011), grey triangles are deciles of the data from
152 Docherty et al., and blue points are measurements from calibration solutions of varying mixtures
153 of NH_4NO_3 and $(\text{NH}_4)_2\text{SO}_4$. Such consistency would be unexpected if a major fraction of the
154 particle NH_4^+ evaporated as intact salts, as suggested by Murphy (2016) (Hu et al., 2017b) .

155



156

157 **Figure S7.** (a) Plot of NH_4 RIE, keeping SO_4 RIE constant, versus the molar fraction of $p\text{NO}_3$
 158 measured in the solution, for calibration solutions of varying mixtures of NH_4NO_3 and $(\text{NH}_4)_2\text{SO}_4$.
 159 (b) Same as (a), but for SO_4 RIE and keeping NH_4 RIE constant. For both figures, the black dots
 160 are the values from the calibrations, the thick red line is the average of all the values, and the
 161 shaded red area is $\pm 1\sigma$.

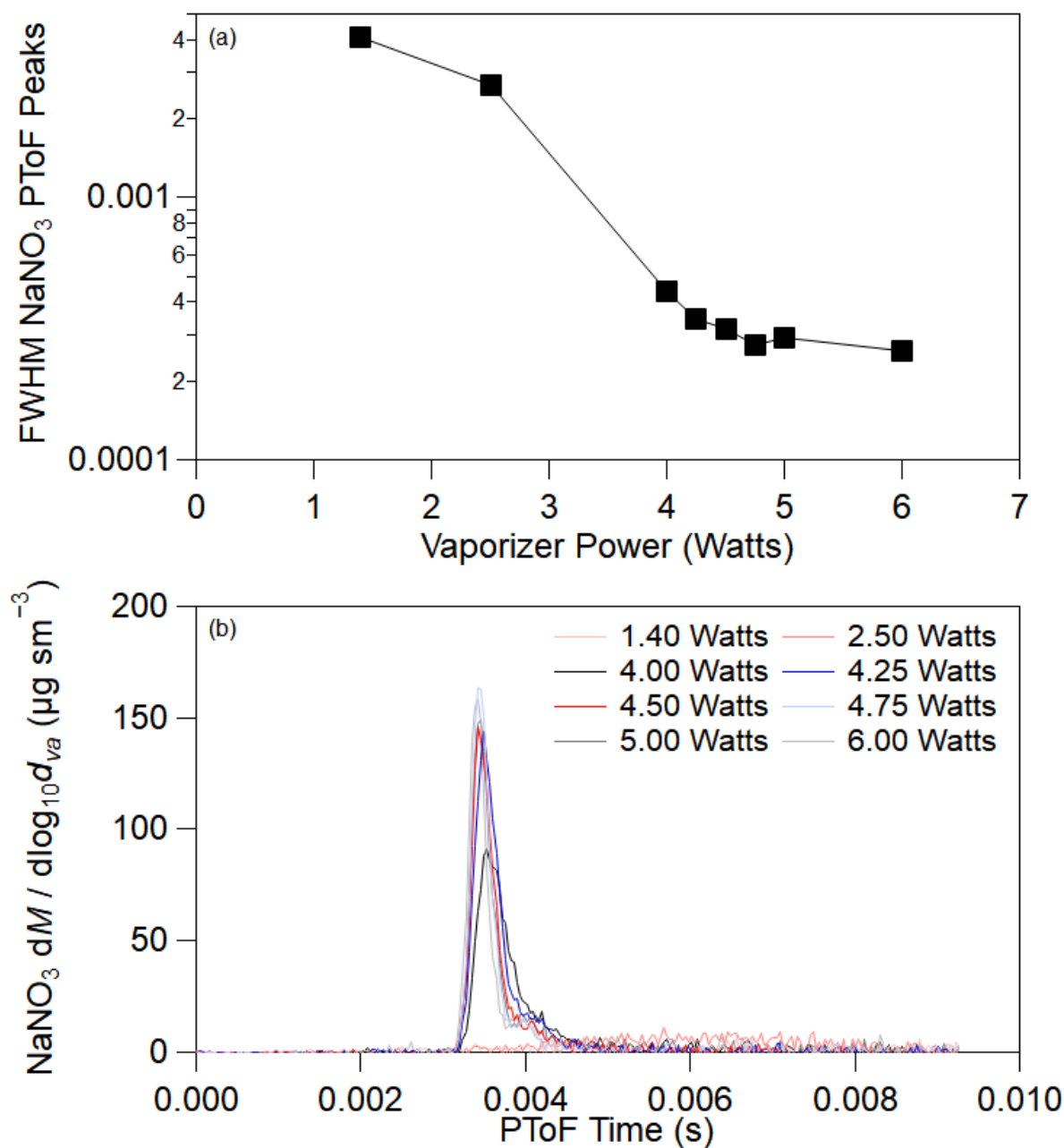


Figure S8. (a) Full-width half-maximum (FWHM) of NaNO_3 size distributions in PToF mode (b) vs. different vaporizer power inputs. See text for further details.

S3. Application of Positive Matrix Factorization (PMF)

Positive matrix factorization analysis (PMF, performed using the CU-Boulder PMF Evaluation Tool PET-Panel v3.00A, http://cires1.colorado.edu/jimenez-group/wiki/index.php/PMF-AMS_Analysis_Guide#PMF_Evaluation_Tool_Software) (Ulbrich et al., 2009) was used to apportion the total OA aerosol into several components. PMF was run on the combined CU-AMS 1 min organic ion matrix for all RFs together during KORUS-AQ. A 6-factor solution was derived with an FPEAK value of 0. Based on comparisons with reference mass spectra from the AMS high-resolution spectral database (<http://cires1.colorado.edu/jimenez-group/HRAMSSd/#Ambient>), comparisons of time series (Figure S9), and correlations with other trace species (Figure S11), the factors were recombined into more-oxidized, oxidized organic aerosol (MO-OOA), less-oxidized, oxidized aerosol (LO-OOA), and hydrocarbon-like organic aerosol (HOA) (Figure S10). HOA correlated with primary emissions (e.g., NO_x, various hydrocarbons) whereas LO-OOA and MO-OOA correlated with secondary photochemical products (e.g., CH₂O, PAN, pNO₃, SO₄). Here, primary OA is defined as the HOA factor and total oxidized OA (OOA) as the LO-OOA plus MO-OOA factors. OOA is assumed to be dominantly composed of secondary organic aerosol, which is supported by its strong correlation with other secondary photochemical products as documented in the paper, as well as by many prior studies (e.g., Jimenez et al., 2009; and references therein).

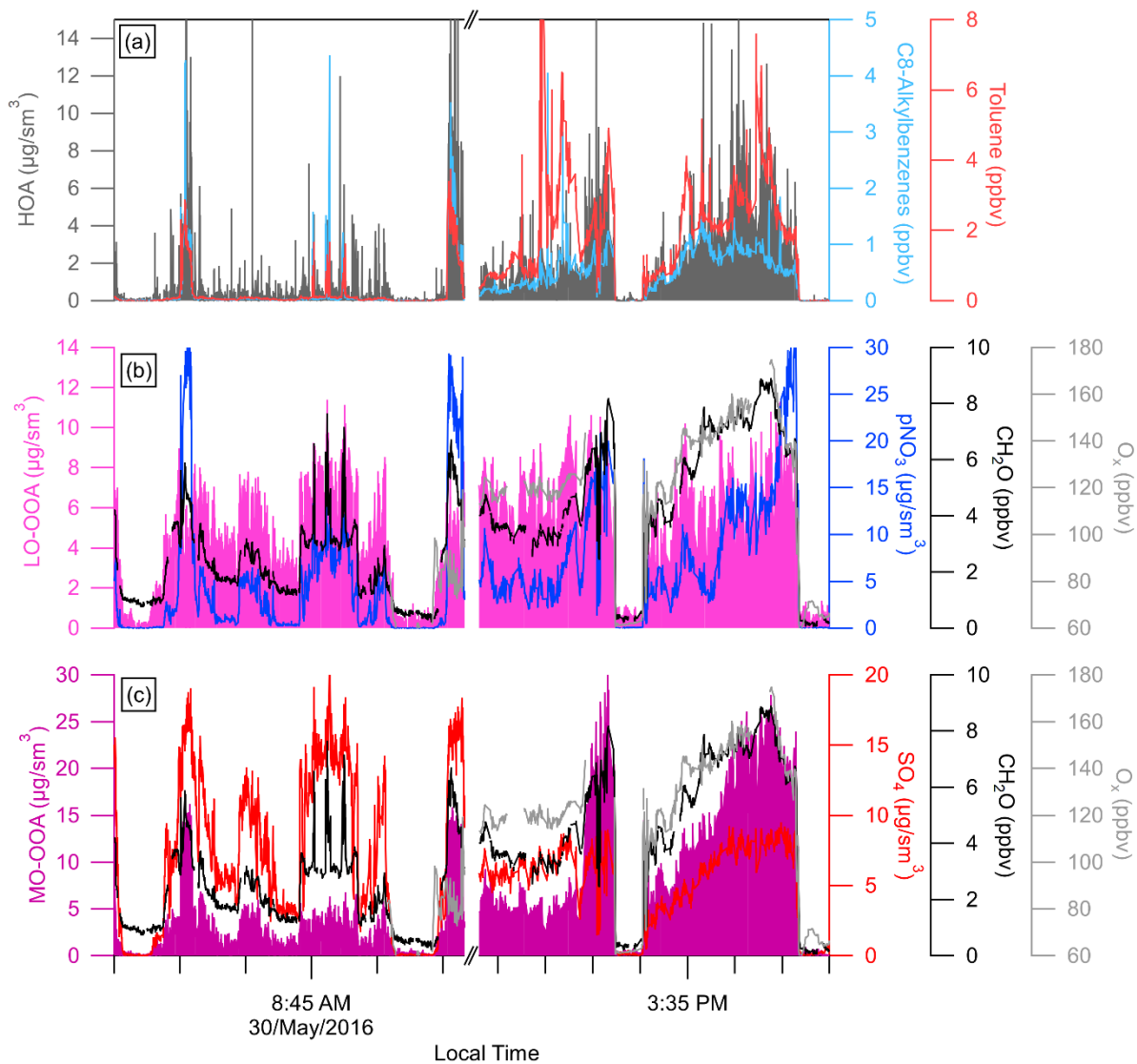
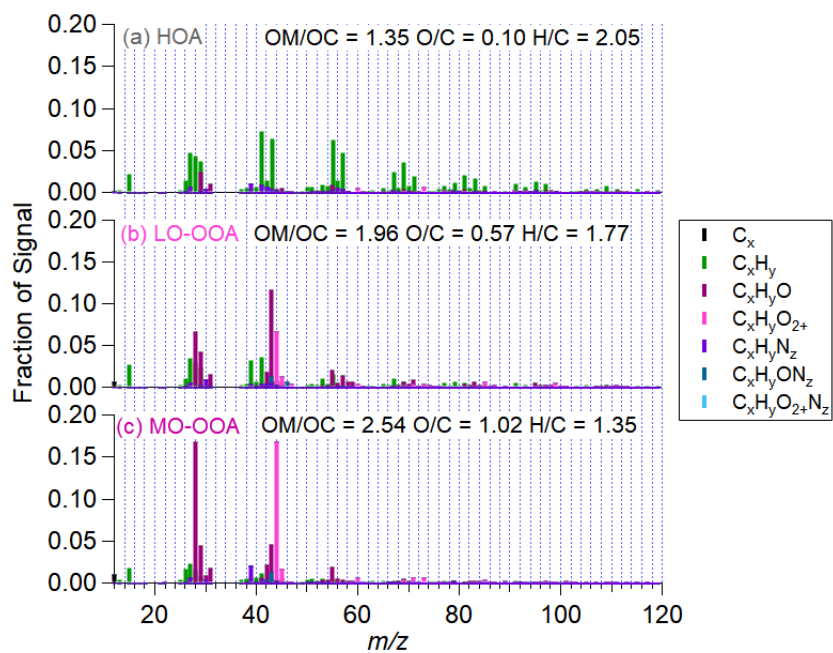


Figure S9. Example time series of the 3 PMF ((a) HOA, (b) LO-OOA, and (c) MO-OOA) results (left axes) and some species that correlate with the corresponding PMF results (right axes) from RF14. The morning and afternoon overpasses over Seoul, South Korea, are shown.



190

191 **Figure S10.** Mass spectra for PMF solution (a) HOA, (b) LO-OOA, and (c) MO-OOA for all of
 192 KORUS-AQ.

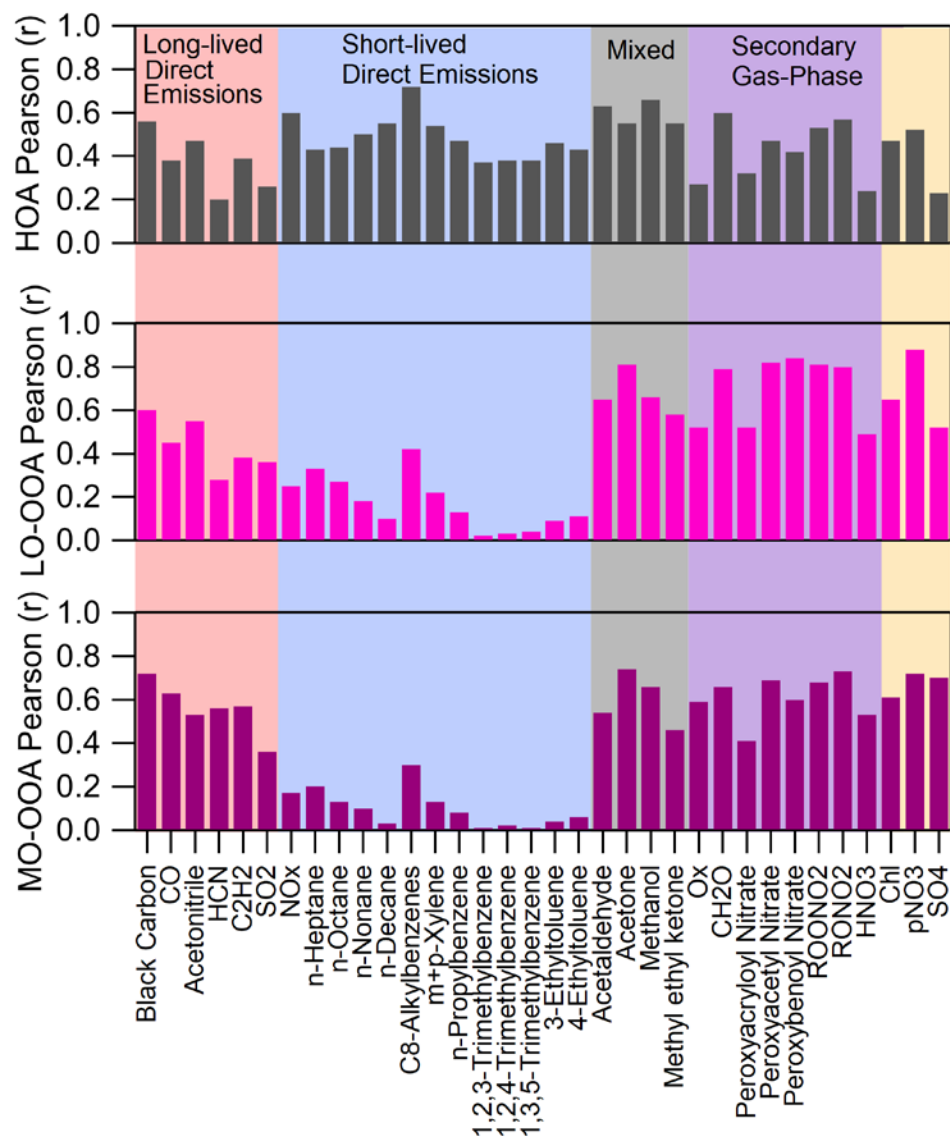
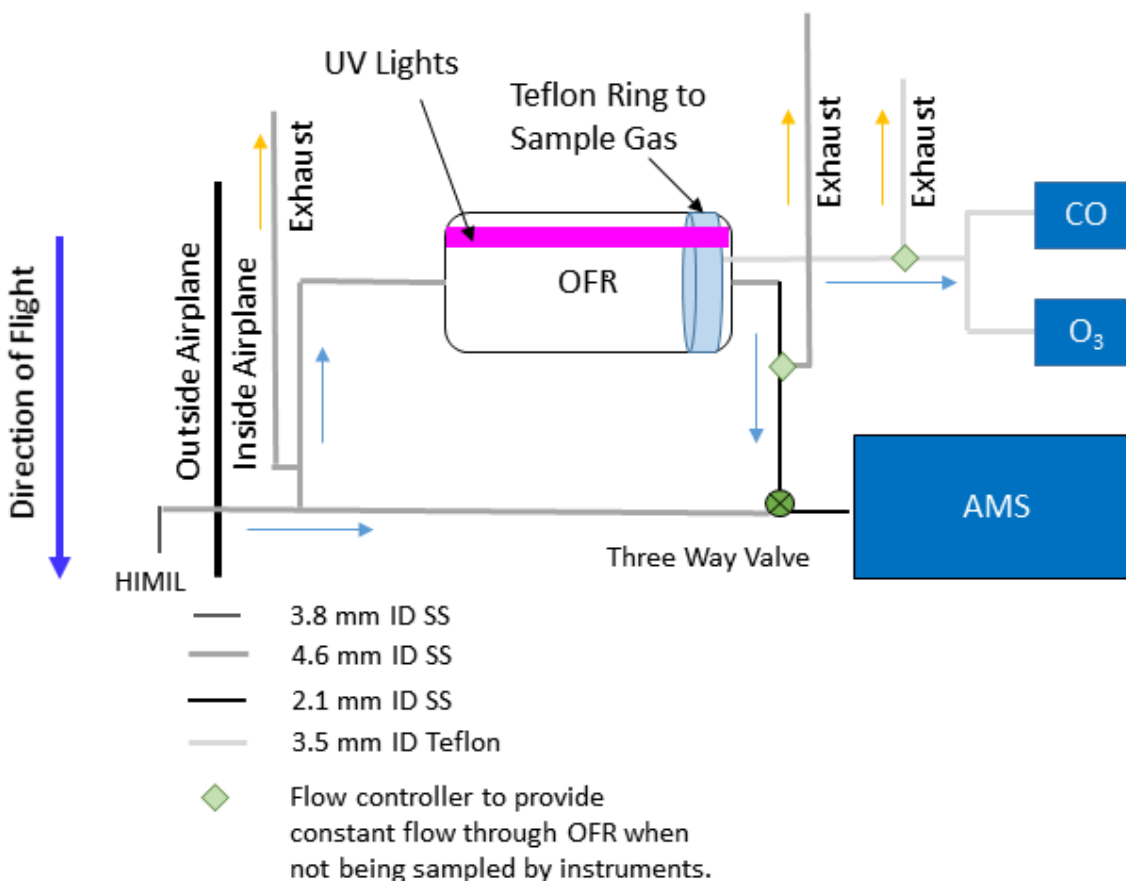


Figure S11. Pearson correlation coefficients for HOA (grey, top), LO-OOA (light pink, middle), and MO-OOA (dark pink, bottom) factors versus species listed in x-axis. The background colors represent the dominant group of sources of the correlating species. The yellow in the far right indicates other PM₁ components measured by the CU-AMS.

199 **S4. Oxidation Flow Reactor (OFR) Sampling**



200

201 **Figure S12.** Schematic of the OFR sampling during KORUS-AQ. UV lamp is represented by the

202 purple light in the OFR. Size and type of tubing is represented in figure, where ID is internal

203 diameter and SS is stainless steel. Tubing distances were always as short as feasible and often

204 shorter than represented, but they are stretched in this drawing for clarity

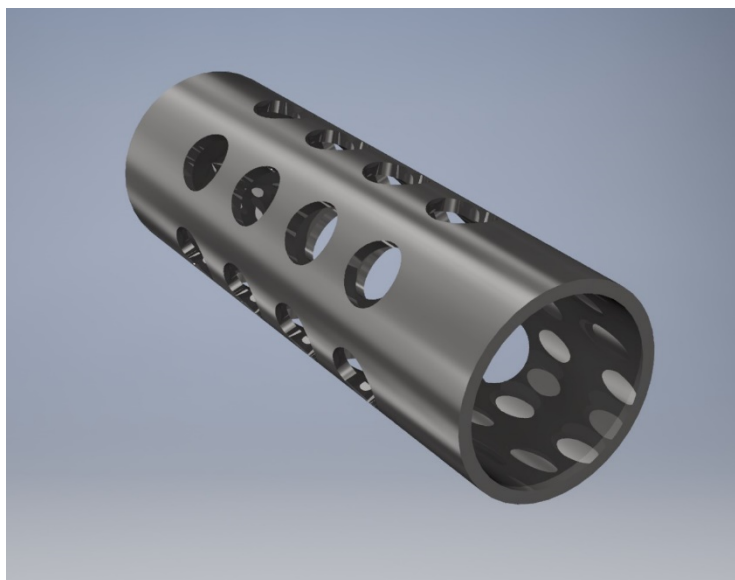


Figure S13. 3D rendition of the computer model of the ½” press fitted stainless steel inlet, coated in SilcoNert (SilcoTek Co, Bellefonte, PA), used in the inlet of the OFR during KORUS-AQ, to avoid “short-circuiting” between the inlet and outlet of the OFR.

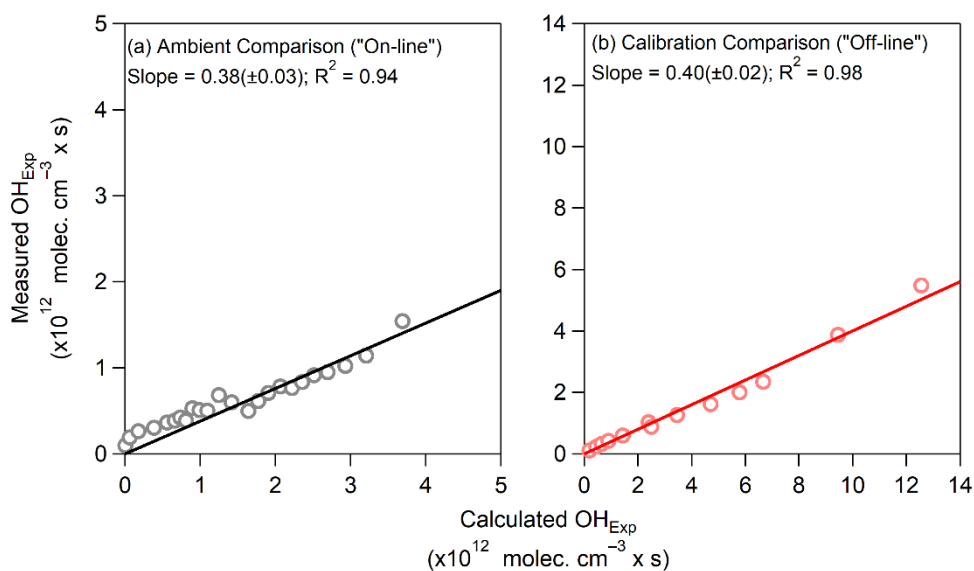


Figure S14. (left) Measured OH_{Exp} from the decay of CO in ambient air (measured by the DACOM instrument, see text) and OFR output air (measured by the Picarro instrument) and (right) measured OH_{Exp} from the decay of CO from a calibration cylinder versus calculated OH_{Exp} using the predictive expression in Peng et al. (2015). The calibration factor determined by this analysis was similar to past studies (Palm et al., 2016) and was applied to all data shown in this paper.

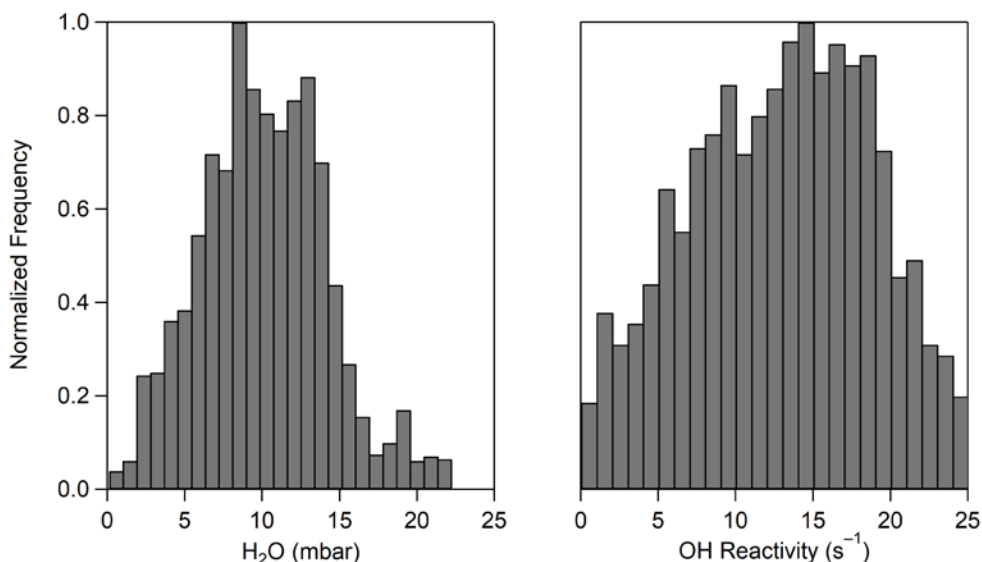


Figure S15. (left) Frequency distribution of water vapor below 2 km during KORUS-AQ. (right) Normalized histogram of measured OH reactivity (OHR) below 2 km during KORUS-AQ.

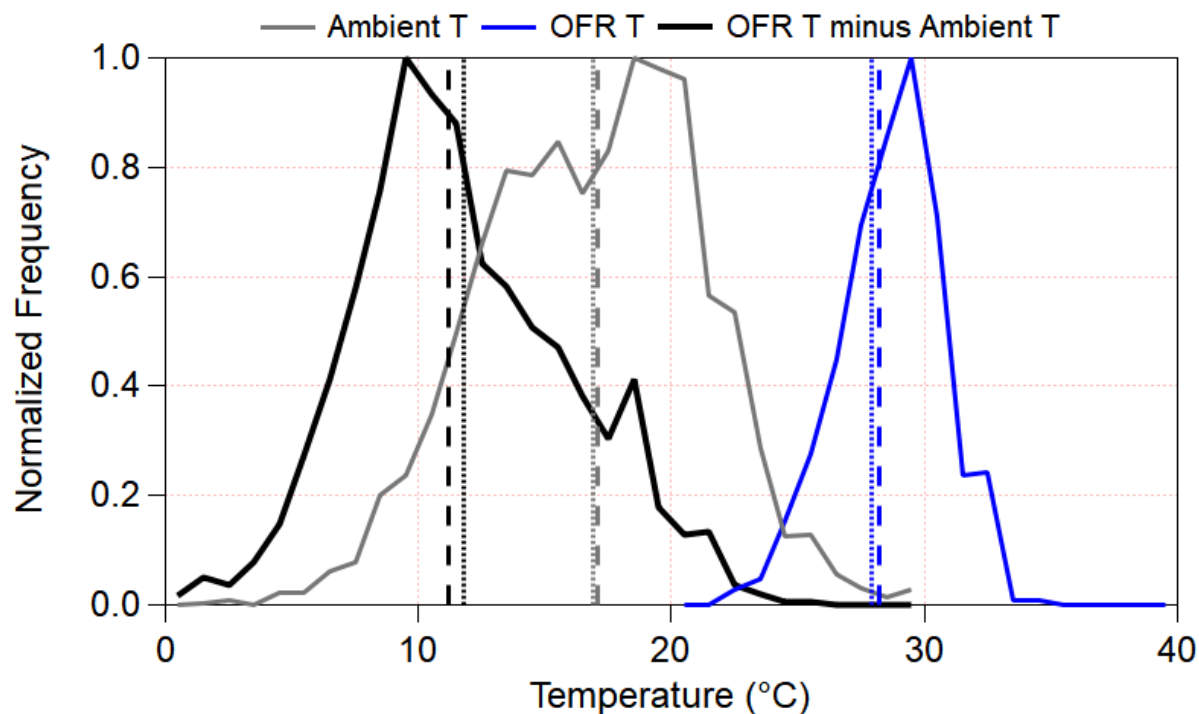


Figure S16. Frequency distribution of the ambient (black), OFR (blue), and difference between OFR and ambient temperature (grey) (°C). Vertical lines show the mean (long-dashed) and median (short-dashed) temperatures for the ambient, OFR, and difference between the two.

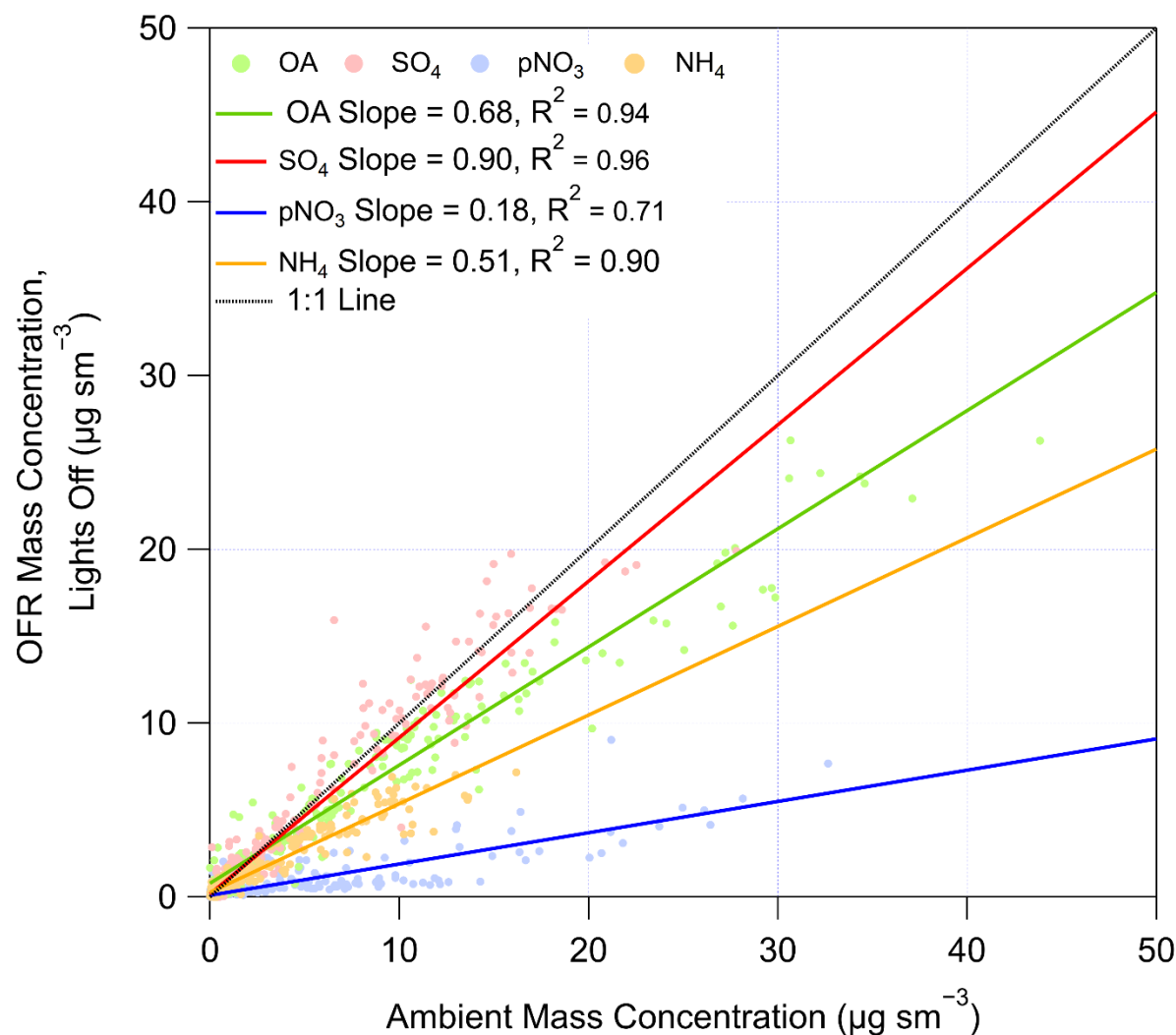


Figure S17. Comparison of organic (green), sulfate (red), nitrate (blue), and ammonium (orange) aerosol sampled through the OFR, with lights off, versus ambient aerosol. Under these conditions the OFR is just acting as a thermal denuder (e.g. Huffman et al., 2009), leading to evaporation of some aerosols due to increased temperature in the aircraft cabin vs. outside. In addition, small particle losses in lines and the OFR are observed for sulfate, which is generally non-volatile. See text for further details and discussion.

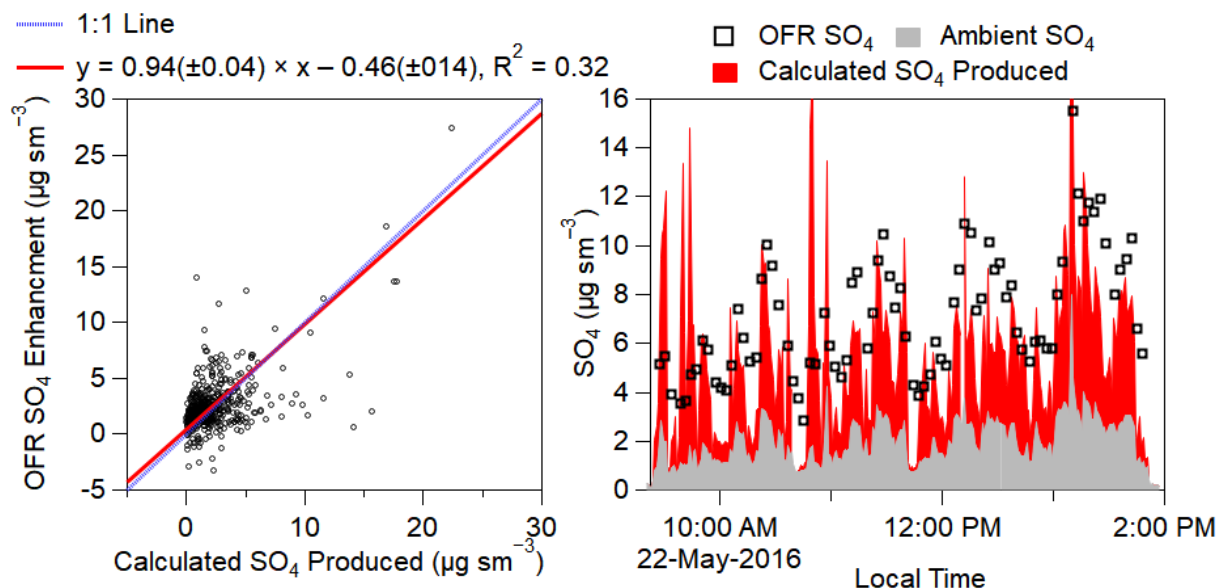


Figure S18. (a) Scatter plot of OFR SO₄ Enhancement (OFR – Ambient) versus calculated SO₄ produced, using SO₂ observations, estimated OH_{exp}, and condensation fate correction. (b) Time series of OFR SO₄ (black squares), ambient SO₄ (light grey), and calculated SO₄ (dark red) for the RF11 flight.

Analysis of CS Values for KORUS-AQ

If we used the condensational sink from just the ambient data, which neglects the added particle surface area formed in the OFR as described in Section 2.4 and Eq. 1 (Ortega et al., 2016; Palm et al., 2016, 2017, 2018), the agreement between calculated and measured SO₄ enhancement decreases to a slope of 0.74 ($R^2 = 0.28$), indicating that the condensational sink is likely too low. This suggests that, to first order, the aerosol surface area, estimated from observations and Eq. 1 (in the main paper), provides a reasonable estimate of the condensational sink within the OFR during KORUS-AQ. Thus, similar to other studies (Ortega et al., 2016; Palm et al., 2016, 2017, 2018), we find, at the typical OH_{exp} in the OFR, that 50 – 60% of the oxidized condensable organic gases are condensing onto aerosol, with 20 – 25% undergoing further reactions with OH leading to highly volatile compounds, 8 – 13% exiting the OFR prior to condensing on aerosol, and 12%

condensing to the wall (Figure S19). Note that the further reactions with OH are not relevant for H_2SO_4 , and thus they have not been included in the analysis shown in in Fig. SI-18.

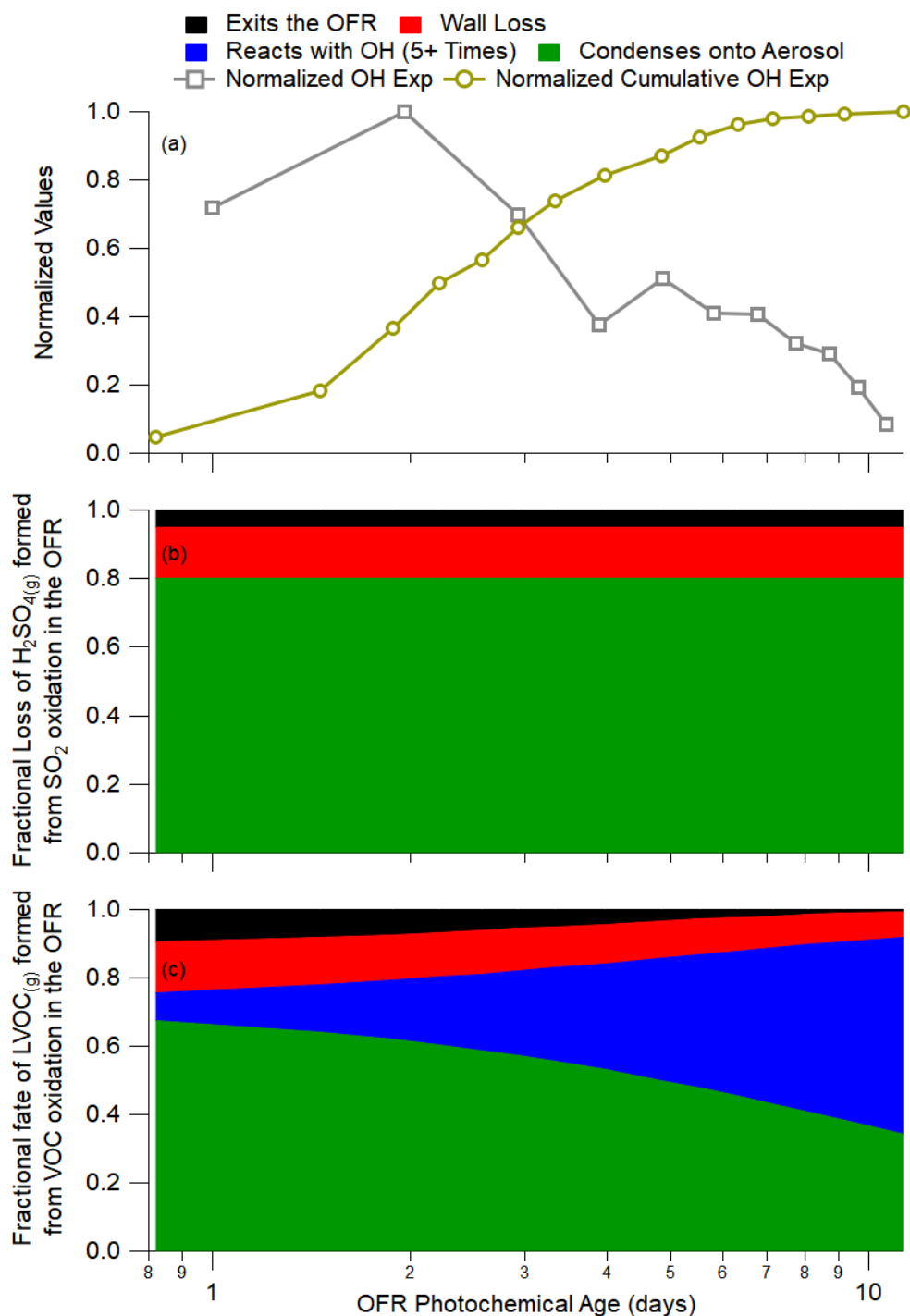


Figure S19. (a) Observed normalized frequency and cumulative frequency of OH Exposure observed during KORUS-AQ in the OFR. (b) Calculated fate of the SO_2 oxidized in the OFR

253 versus OFR OH Exposure. (c) Calculated fate of low-volatility condensable vapors (formed from
254 VOC oxidation) versus OFR OH Exposure. For (b) and (c), the losses include flowing through the
255 OFR without condensing onto aerosol (black), condensing onto the wall (red), condensing onto
256 the aerosol (assuming a median value of 85.8 s, green), and reacting with OH enough to make it
257 too volatile to condense onto aerosol (blue).

258

S5. Calculation of Photochemical Age over Seoul, South Korea

The photochemical clock calculations used throughout this work are described here. The rate constants used for these clocks are located in SI Table 3. For the NO_x/NO_y photochemical clock (e.g., Kleinman et al., 2007) (herein referred to as the NO_x photochemical clock), Eq. S1 is used, with the updated rate constant from Mollner et al. (2010).

$$t = \frac{\ln\left(\frac{NO_x}{NO_y}\right)}{k_{OH+NO_2}[OH]} \quad (S1)$$

where t is the time, in days, [OH] is assumed to be 1.5×10^6 molecules/cm³ (for standardization), and NO_x and NO_y are the chemiluminescence measurements. The NO_x clock is used for photochemical ages less than 1 day to (1) reduce the effect of loss of HNO₃ and other oxidized reservoirs due to deposition (lifetime ~6 hours) (Neuman et al., 2004; Nguyen et al., 2015; Romer et al., 2016) and (2) to ensure that t was still sensitive (and precise) to the NO_x and NO_y concentrations (~20% of NO_x still remaining at $t = 1$ day).

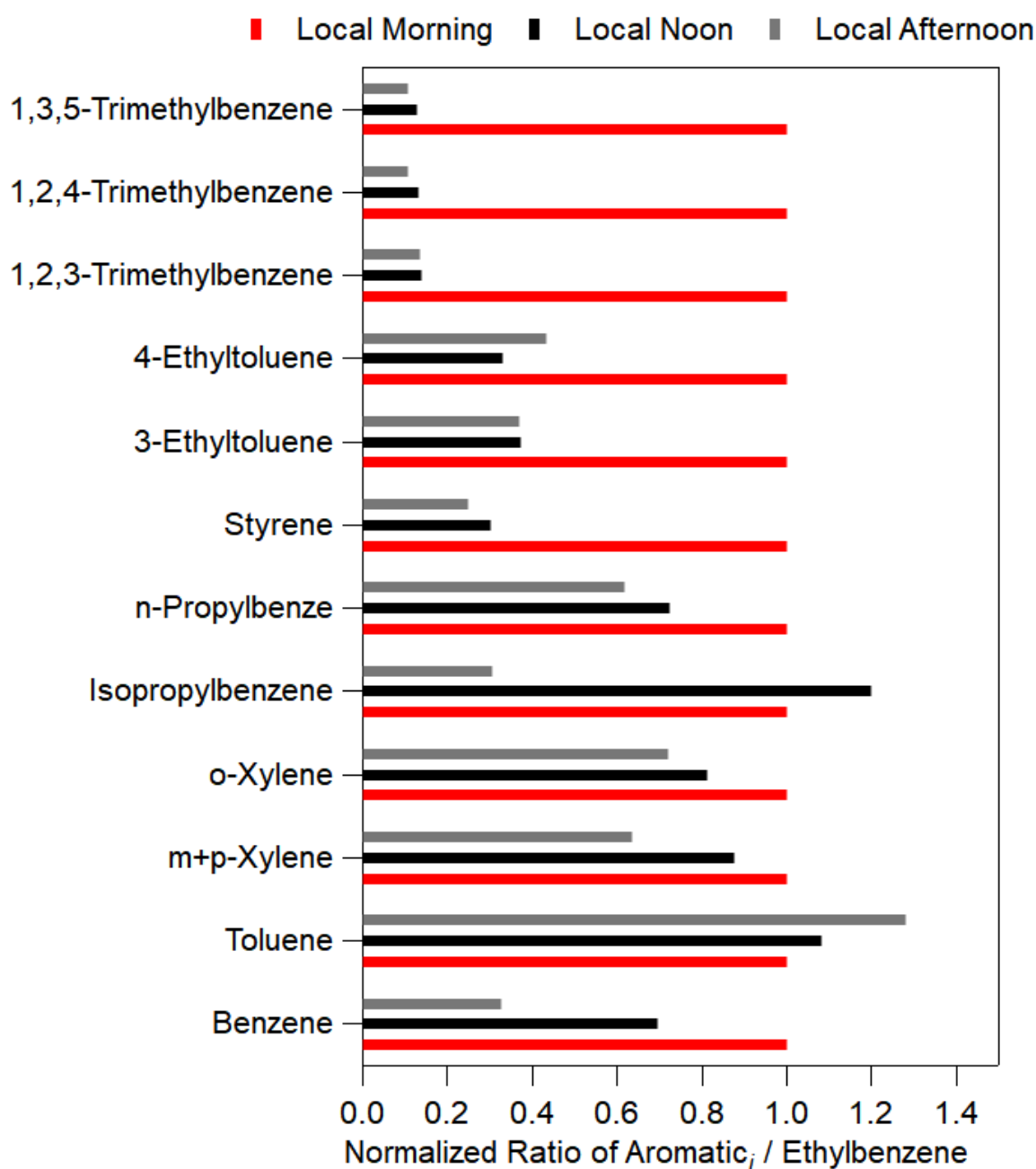
For the aromatic photochemical clock over Seoul, the more reactive aromatics (ethylbenzene in the denominator) are utilized, which should be more sensitive to the short photochemical aging observed over Seoul (Parrish et al., 2007), along with Eq. SS2.

$$t = -\frac{1}{[OH] \times (k_{aromatic_i} - k_{ethylbenzene})} \times \left(\ln\left(\frac{aromatic_i(t)}{ethylbenzene(t)}\right) - \ln\left(\frac{aromatic_i(0)}{ethylbenzene(0)}\right) \right) \quad (S2)$$

where t is the time, in hours, the k 's are the corresponding OH rate constants for each aromatic compound (SI Table 3), and the third term $\left(\ln\left(\frac{aromatic_i(0)}{ethylbenzene(0)}\right)\right)$ corresponds to the emission ratios for those two aromatic compounds. Similar to the NO_x clock, we assume [OH] = 1.5×10^6 molecules/cm³ for standardization. The aromatics measurements used in this calculation are from WAS.

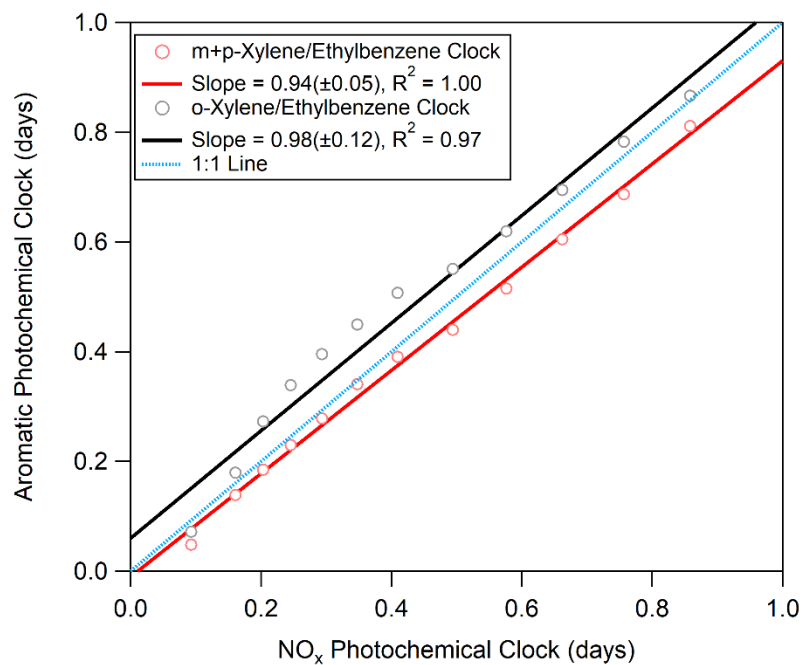
To evaluate which aromatic compounds to use in the clock, the behavior of the ratios of each aromatic compound with ethylbenzene versus the three missed approaches (morning, noon, and afternoon) over Seoul during KORUS-AQ (Figure S20) are compared. The idea is that if the 2 aromatic compounds are co-emitted, the ratios should be removed proportionally to their OH rate constants. E.g. for faster reacting compounds (e.g., o-xylene), the ratio to ethylbenzene should decrease with time as more o-xylene was consumed, compared to ethylbenzene, by OH (de Gouw et al., 2017). On the other hand, for slower reacting compounds (e.g., toluene), the ratio to ethylbenzene should increase with time as more ethylbenzene was consumed by OH. Also, this analysis provides an indication of which ratios would provide meaningful results throughout the entire day (de Gouw et al., 2017). Ideally, there should be a decrease with each later missed approach, and not a leveling off after two missed approaches (e.g., the trimethylbenzenes and ethyltoluenes). Only the m+p-xylene/ethylbenzene and o-xylene/ethylbenzene ratios meet this criterion. Finally, to determine the emission ratios, we calculated what the m+p-xylene/ethylbenzene and o-xylene/ethylbenzene ratio was for observations where the NO_x photochemical was less than 0.07 days (corresponding to less than 10% of either species being consumed). Comparing these two aromatic clocks to the NO_x photochemical clock (Figure S21), a similar agreement between the two aromatic clocks with the NO_x photochemical clock was observed, providing confidence in using all three clocks to calculate photochemical age to evaluate OA production over Seoul. For the remainder of the paper, we mainly use the NO_x photochemical clock to eliminate the uncertainty of the emission ratios, unless otherwise noted.

Finally, for observations over the Yellow Sea, the aromatic clock (Eq. SS2) was used, but benzene and toluene were used since these air masses are more photochemically processed (Parrish et al., 2007). For the emission ratios, values reported by Yuan et al (2013) were used.



304

305 **Figure S20.** Comparison of various aromatic compounds/ethylbenzene ratios sampled over Seoul,
 306 South Korea, during KORUS-AQ. The ratios are normalized by the morning ratios.



307
 308 **Figure S21.** Binned scatter plot of the aromatic photochemical clock ages versus NO_x
 309 photochemical clock ages for all observations over Seoul. All ages are normalized to $\text{OH} = 1.5 \times 10^6$
 310 molecules/ cm^3 .

311 **Table S3.** Rate constants used throughout this study. Unless noted otherwise, rate constants
 312 without temperature dependence only have a value measured at 298 K.

Reaction	Rate Constant (cm ³ /molecules/s)	Reference
<i>Inorganic</i>		
CO	$2.28 \times 10^{-13,a}$	Sander et al. (2011)
NO ₂	$1.23 \times 10^{-11,a}$	Mollner et al. (2010)
SO ₂	$8.94 \times 10^{-13,a}$	Atkinson et al. (2004)
<i>Alkanes</i>		
Ethane	$6.9 \times 10^{-12} \times \exp(-1000/T)$	Atkinson et al. (2006)
Propane	$7.6 \times 10^{-12} \times \exp(-585/T)$	Atkinson et al. (2006)
n-Butane	$9.8 \times 10^{-12} \times \exp(-425/T)$	Atkinson et al. (2006)
i-Butane	$1.17 \times 10^{-17} \times T^2 \times \exp(213/T)$	Atkinson (2003)
n-Pentane	$2.52 \times 10^{-17} \times T^2 \times \exp(158/T)$	Atkinson (2003)
i-Pentane	3.6×10^{-12}	Atkinson (2003)
n-Hexane	$2.54 \times 10^{-14} \times T \times \exp(-112/T)$	Atkinson (2003)
Methyl-cyclopentane	7.65×10^{-12}	Sprengnether et al. (2009)
Cyclohexane	$3.26 \times 10^{-17} \times T^2 \times \exp(262/T)$	Atkinson (2003)
Methyl-cyclohexane	9.43×10^{-12}	Sprengnether et al. (2009)
n-Heptane	$1.95 \times 10^{-17} \times T^2 \times \exp(406/T)$	Atkinson (2003)
n-Octane	$2.72 \times 10^{-17} \times T^2 \times \exp(361/T)$	Atkinson (2003)
n-Nonane	$2.53 \times 10^{-17} \times T^2 \times \exp(436/T)$	Atkinson (2003)
n-Decane	$3.17 \times 10^{-17} \times T^2 \times \exp(406/T)$	Atkinson (2003)
<i>Alkenes</i>		
Ethylene	$7.84 \times 10^{-12,a}$	Atkinson et al. (2006)
Propene	$2.86 \times 10^{-11,a}$	Atkinson et al. (2006)
1-butene	$6.6 \times 10^{-12} \times \exp(465/T)$	Atkinson et al. (2006)
i-butene	$9.4 \times 10^{-12} \times \exp(505/T)$	Atkinson et al. (2006)
cis-butene	$1.1 \times 10^{-11} \times \exp(485/T)$	Atkinson et al. (2006)
trans-butene	$1.0 \times 10^{-11} \times \exp(553/T)$	Atkinson et al. (2006)
1,3-butadiene	$1.48 \times 10^{-11} \times \exp(448/T)$	Atkinson and Arey (2003)
<i>Aromatics</i>		
Benzene	$2.3 \times 10^{-12} \times \exp(-190/T)$	Atkinson et al. (2006)
Toluene	$1.8 \times 10^{-12} \times \exp(340/T)$	Atkinson et al. (2006)
Ethylbenzene	7×10^{-12}	Atkinson and Arey (2003)
Isopropylbenzene	6.3×10^{-12}	Atkinson and Arey (2003)
n-propylbenzene	5.8×10^{-12}	Atkinson and Arey (2003)
Styrene	5.8×10^{-11}	Atkinson and Arey (2003)
m+p-xylene	$1.87 \times 10^{-11,b}$	Atkinson and Arey (2003)
o-xylene	1.36×10^{-11}	Atkinson and Arey (2003)
1,3,5-trimethylbenzene	$1.32 \times 10^{-11} \times \exp(450/T)$	Bohn and Zetzsch (2012)
1,2,3-trimethylbenzene	$3.61 \times 10^{-12} \times \exp(620/T)$	Bohn and Zetzsch (2012)
1,2,4-trimethylbenzene	$2.73 \times 10^{-12} \times \exp(730/T)$	Bohn and Zetzsch (2012)
3-Ethyltoluene	1.2×10^{-11}	Atkinson and Arey (2003)
4-Ethyltoluene	1.2×10^{-11}	Atkinson and Arey (2003)
<i>S/IVOCs</i>		

S/IVOC	2×10^{-11}	Ma et al. (2017)
<i>Biogenics</i>		
Isoprene	$2.7 \times 10^{-11} \times \exp(390/T)$	Atkinson et al. (2006)
α -pinene	$1.2 \times 10^{-11} \times \exp(440/T)$	Atkinson et al. (2006)
β -pinene	$1.55 \times 10^{-11} \times \exp(467/T)$	Atkinson and Arey (2003)
<i>Radicals</i>		
NO + RO ₂	$2.8 \times 10^{-12} \times \exp(300/T)$	Sander et al. (2011)
HO ₂ + RO ₂	$4.1 \times 10^{-13} \times \exp(750/T)$	Sander et al. (2011)
RO ₂ + RO ₂	$9.5 \times 10^{-14} \times \exp(390/T)$	Sander et al. (2011)

^aShowing the rate constant at 298 K, 1013 hPa. However, for this study, we used the temperature and pressure dependent formulation listed in each respective reference.

^bThis is the average of m-xylene and p-xylene rate constants.

S6. Potential SOA Calculations

To determine the amount of SOA produced from the observed precursors, Eq. S3 was used, where Y is the stoichiometric aerosol yield for each hydrocarbon (RH) species i , similar to other studies (e.g., Zhao et al., 2014). The updated yields from Ma et al. (2017) were used, which incorporate a correction for the gas-phase partitioning of semi-volatile compounds to chamber walls (Krechmer et al., 2016). Since there were no direct measurements of S/IVOC concentrations, an estimated (Robinson et al., 2007; Dzepina et al., 2009) relationship between the amount of gas-phase S/IVOC co-emitted with POA at the typical temperatures ($\sim 20^\circ\text{C}$) and OA mass concentrations ($\sim 10 \mu\text{g sm}^{-3}$) observed over Seoul were used. The POA is taken from Figure 5b and is within the range of values observed in other urban environments (Zhang et al., 2005; Hayes et al., 2013; Ait-Helal et al., 2014; Kim et al., 2018) ($13 \mu\text{g sm}^{-3} \text{ ppmv}^{-1}$ in Seoul versus $4.5 - 28.8 \mu\text{g sm}^{-3} \text{ ppmv}^{-1}$ in other studies).

$$P(OA) = \sum_i Y_i \times \Delta RH_i \quad (\text{S3})$$

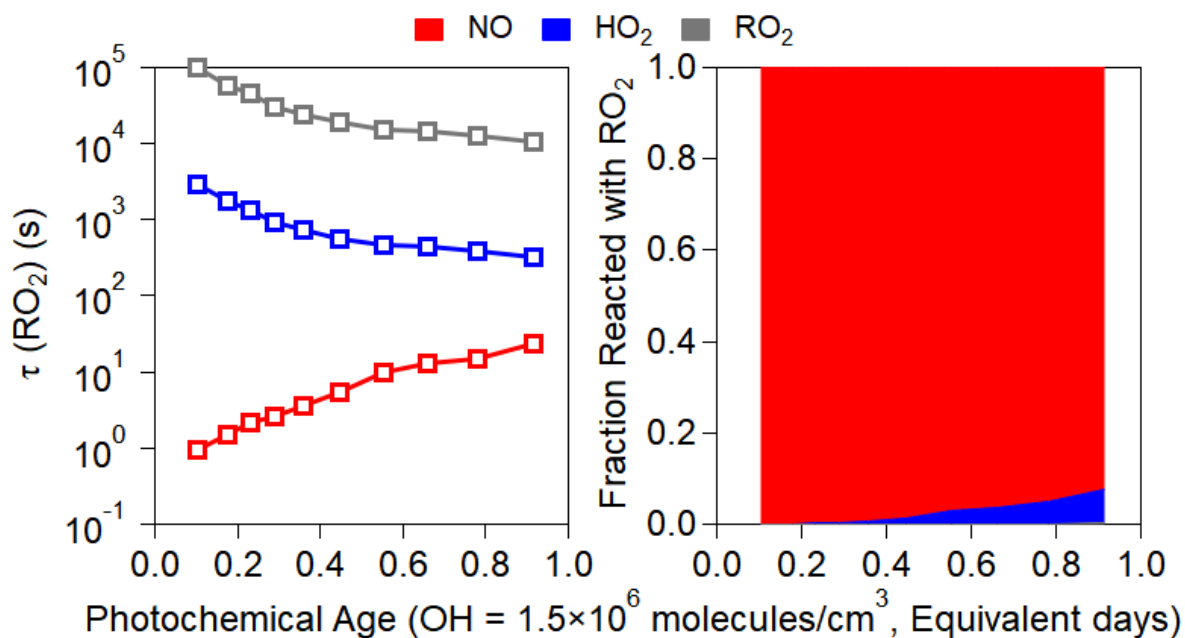
$$\Delta RH = \frac{RH(t)}{e^{(-k[OH]t)}} - RH(t) \quad (\text{S4})$$

The hydrocarbons measured on the DC-8 were the concentrations at time, t ; thus, Eq. S4 was used, which takes into account the amount of OH that oxidized the hydrocarbon ($\text{OH}_{\text{exp}} =$

[OH] t) between emissions and measurement, and k is the OH rate constant for each specific hydrocarbon (SI Table 3).

Finally, to determine the fate of the RO₂ radical in the reactions over Seoul (high/low NO_x regime), and thus, what aerosol yields to use, the RO₂ lifetime with reaction of NO, HO₂, and RO₂ versus photochemical age was calculated (Figure S22). The measured NO and HO₂ was used in the calculations, we assumed RO₂ was approximately the same concentration as HO₂ in this calculation (Thornton et al., 2002), and the rate constants in SI Table 3 were used to calculate the lifetime and fractional fate of RO₂. The fate of RO₂ with autoxidation is not included as the rate is still uncertain (Crounse et al., 2013) and it should be less important in highly polluted environments such as Seoul, especially at the lower photochemical ages (< 0.5 eq. days) where most SOA is observed to be formed. The dominant sink of RO₂ over Seoul during KORUS-AQ is the reaction with NO, suggesting that the SOA yields for “high NO” conditions should be used to describe the production of SOA.

346



347

348 **Figure S22.** (left) Lifetime of RO_2 due to reactions with NO (red), HO_2 (blue), and RO_2 (grey)
 349 versus NO_x photochemical clock, normalized by $\text{OH} = 1.5 \times 10^6$ molecules/ cm^3 . (right) Fraction of
 350 RO_2 reacting with NO (red), HO_2 (blue), or RO_2 (red) versus NO_x photochemical clock,
 351 normalized by $\text{OH} = 1.5 \times 10^6$ molecules/ cm^3 . Values are calculated using observations over Seoul,
 352 South Korea, during KORUS-AQ, and RO_2 is assumed to be approximately equal to HO_2
 353 (Thornton et al., 2002).

S7. FLEXPART Source Analysis

Source contributions have been estimated using Lagrangian backtrajectory calculations with the FLEXPART-WRF model (Brioude et al., 2013) in version 3.3.1, driven by meteorological output from NCEP GFS (NCEP) analyses downscaled to 5 km horizontal resolution using the Weather Research and Forecasting (WRF) model (Skamarock et al., 2008) in combination with the CREATE emission inventory (Woo et al., 2013). Approximately 20,000 parcels are released in 1 min intervals from the then-current location of the DC-8 during its research flights and parcel trajectories are followed back in time for 24 hours. The total time parcels spent in the lowermost 100 m—as surrogate for air having contact with an emission source at the ground—is recorded (residence time, [$\text{s kg}^{-1} \text{ m}^3$]) and then folded with the emission fluxes ($[\text{kg m}^{-2} \text{ s}^{-1}]$) given by the CREATE inventory for different compounds and source regions. This delivers an estimate of the source contribution (as increment in volume mixing ratio at the receptor, i.e., the DC-8 location) of the emissions of a given compound from a given region, assuming a perfect transport simulation and an inert compound.

S8. Intercomparisons of CU-AMS with Other Measurements on the NASA DC-8

We evaluate the measurement comparisons of the CU-AMS versus other aerosol measurements on-board the DC-8 during KORUS-AQ. We start with the mist chamber / ion chromatograph instrument (MC/IC), which has a comparable size cut as the AMS. The comparisons for SO_4 show good correlation ($R^2 = 0.76$) and slope close to 1 (0.95) (Figure S23). The higher scatter for the MC/IC is thought to arise from the lag and smearing in the measurements that has been observed in prior studies (TAbMET, 2009). For example, the correlation between instruments without lag and smearing have R^2 of 0.87 – 0.91 (CU-AMS versus extinction and CU-AMS vs K-AMS for certain RFs). If the MC/IC and CU-AMS SO_4 measurements are averaged to the sampling frequency of the University of New Hampshire filters (not shown), the R^2 improves (0.82) with no impact on the slope.

The comparison between the UNH filters and CU-AMS SO_4 shows higher R^2 (0.86) but lower slope (0.80), compared to MC/IC vs. CU-AMS. The higher R^2 is likely due to longer averaging time and lack of smearing that occurred with the MC/IC. As a comparison, the R^2 between MC/IC and filters are 0.84. The lower slope for the filters than the MC/IC is thought to be due to the different size cut-offs for the two measurements. For the filters, the upper size cut-off is $\sim 4 \mu\text{m}$ (McNaughton et al., 2007); whereas, the upper size cut-off for the MC/IC is comparable to the AMS aerosol size cut-off ($\sim 1 \mu\text{m}$ aerodynamic). This means that the filter samples may include SO_4^{2-} from sea salt (sodium and calcium) and dust (calcium) (Heo et al., 2009; Kim et al., 2016; Heim et al., 2018). This is shown in Figure S24 and described in detail in Heim et al. (2018). Heim et al. (2018) found that dust dominated supermicron aerosol for approximately half of the campaign, and during these periods, supermicron SO_4^{2-} accounted for $\sim 50\%$ of the total SO_4^{2-} (sub plus supermicron). Taken together, the comparisons of SO_4 mass

concentrations from the CU-AMS from these two different methods (filter and MC/IC) indicate that the CU-AMS quantitatively captures the concentrations of SO₄.

Next, we compare the non-refractory species concentrations measured by the CU- and K-AMS. Intercomparisons between these two measurements for a few flights have been presented in prior publications (Hu et al., 2018a, 2018b). The K-AMS used a capture vaporizer, which leads to CE of ~1 for all ambient species (Hu et al., 2017a, 2017b; Xu et al., 2017). Here, we investigate the entire campaign. As shown in Figure S25, $R^2 > 0.80$ for all five species, and all slopes fall within $\pm 20\%$ of unity, which is within the combined uncertainty of both AMSs (~27%). However, at high concentrations (greater than $\sim 5 - 10 \mu\text{g sm}^{-3}$), the scatter between the two measurements increases, and for some species (e.g., SO₄), there is a slight curvature in the comparisons, where CU-AMS is greater than K-AMS. We believe this discrepancy originated from differences in transmission vs. particle size through the aerosol inlet and focusing lens (Figure S26). In-field calibrations showed that The K-AMS had 50% transmission at 615 nm (vacuum aerodynamic diameter; DeCarlo et al. (2004)), compared to the CU-AMS 50% transmission occurring at 900 nm. The reasons for the smaller transmission of the K-AMS are likely related to the PCI design (Bahreini et al., 2008, 2009) or possibly an underperforming aerodynamic lens in K-AMS (Liu et al., 2007). It was found that, in general, the RFs could be split between RFs generally below the K-AMS size cut-off (RFs 1 – 9, 11, 15, and 19) and above the size cut-off (RFs 10, 12 – 14, 16 – 18, 20) (Figure S27). The slopes and R^2 greatly improves for the observations below the K-AMS cut-off versus above (for slopes, 1.02 versus 0.84 and for R^2 , 0.91 versus 0.82).

Finally, the ratios of the total AMS PM₁ masses measured by CU-AMS and K-AMS remain nearly constant about one (within $\pm 11\%$) for the entire campaign and show no trend with estimated CE (for the standard vaporizer only) using the Middlebrook et al. (2012) algorithm (Figure S28).

Thus, when accounting for transmission effects, the two AMSs agree to within 10%, and the CU-AMS agrees to within 20% with the other co-located aerosol mass concentration measurements (filters and MC/IC) on the DC-8. This provides overall confidence in the calculated CE for the standard vaporizer (Middlebrook et al., 2012), RIE, and transmission of PM_{10} for the CU-AMS measurements.

Besides directly comparing species mass, another well-established method to investigate aerosol instrument quantification is to compare the measured PM_{10} mass (CU-AMS plus BC from SP2) versus the submicron extinction measured using methods described in Section 2.3.2 (nephelometer for scattering and absorption by PSAP) (e.g., DeCarlo et al., 2008). During KORUS-AQ, the slope between mass and extinction is $6.00 \text{ m}^2 \text{ g}^{-1}$ (Figure S29) with an R^2 of 0.87. The high correlation and similar slope compared to prior comparisons (Hand and Malm, 2007; DeCarlo et al., 2008; Dunlea et al., 2009; Shinozuka et al., 2009; Liu et al., 2017) indicates that the CU-AMS was not substantially impacted by the aerosol transmission effects discussed above. Also, the strong correlation ($R^2 = 0.87$) between the two instruments, which both have comparable, very high time resolution, indicate that the CU-AMS did not experience any plume recovery artifacts that were observed with the MC/IC or artifacts in measuring highly concentrated plumes.

Finally, we compare the PM_{10} volume concentrations estimated from the LAS PM_{10} versus the CU-AMS plus SP2. For this comparison, we use the calibrated AMS transmission curve during this campaign (Figure S30), which is consistent with those from recent studies (Knote et al., 2011; Hu et al., 2017b), to correct for particle transmission differences between the instruments. The LAS diameters were corrected by a factor of 1.115 from the PSL-calibrated values, to account for the lower refractive index of ambient particles, similar to Liu et al. (2017). To estimate the volume concentration from the combined AMS and BC measurements, we assume additive species

volumes (DeCarlo et al., 2004). Species densities of 1.78 g cm^{-3} for NH_4 , pNO_3 , and SO_4 (Lide, 1991; Salcedo et al., 2006), 1.52 g cm^{-3} for Chl (Lide, 1991; Salcedo et al., 2006), 1.77 g cm^{-3} for BC (Park et al., 2004), and the OA density is estimated from the CU-AMS O/C and H/C ratios of OA using the parameterization of Kuwata et al. (2012). The comparison between total PM_{10} volume estimated from the CU-AMS plus BC vs. versus LAS shows a correlation (R^2) of 0.86. However, the volume from AMS plus SP2 is higher (slope of 1.56) when comparing all of KORUS-AQ. We hypothesize that this may be due to saturation of the LAS detector at high particle concentrations that were frequently observed in this campaign (greater than $1800 \text{ particles cm}^{-3}$ or total CU-AMS plus SP2 mass greater than $40 \text{ } \mu\text{g sm}^{-3}$), as has been observed in prior comparisons (Liu et al., 2017), or a change in the refractive index when OA becomes dominant at these high concentrations (Moise et al., 2015). Different filters are tested and shown in Figure S30 and Figure S31, using both values reported in literature and values that represent a stable ratio between LAS and calculated CU-AMS plus SP2 volume. If we filter for data when there is less than $20 \text{ } \mu\text{g sm}^{-3}$, the slope drops to 1.00, showing agreement between within the combined uncertainties ($R^2 = 0.79$), and providing strong evidence that LAS saturation at higher concentrations is the main reason for the apparent disagreement when analyzing the entire campaign.

We further investigate (Figure S31) whether the slope could be due to LAS saturation or a bias in RIE_{OA} , or in CE, vs. the values used in our analyses (Jimenez et al., 2016; Xu et al., 2018). There is a slight increase in the ratio of AMS plus SP2 to LAS volumes versus OA/total CU-AMS mass at high fractions of OA, although still within the combined measurement uncertainties. With filtered data (less than $1600 \text{ particles cm}^{-3}$ or total CU-AMS mass less than $20 \text{ } \mu\text{g sm}^{-3}$), the volume ratios remain nearly flat, even at high $f(\text{OA})$. This confirms that LAS saturation is the most likely cause for the differences. Finally, a recent study (Xu et al., 2018) has reported new laboratory

measurements of $\text{RIE}_{\text{OA}} = 1.6 \pm 0.5$, although these authors indicated that it was unclear whether this value was applicable to ambient particles, and the value of $\text{RIE}_{\text{OA}} = 1.4$ used in this study is well within their reported uncertainty. When using $\text{RIE}_{\text{OA}} = 1.6$ in our analysis (not shown) the slope for the entire dataset decrease by only 6% (1.56 to 1.47), indicating that RIE uncertainties cannot explain the bulk of the observed difference.

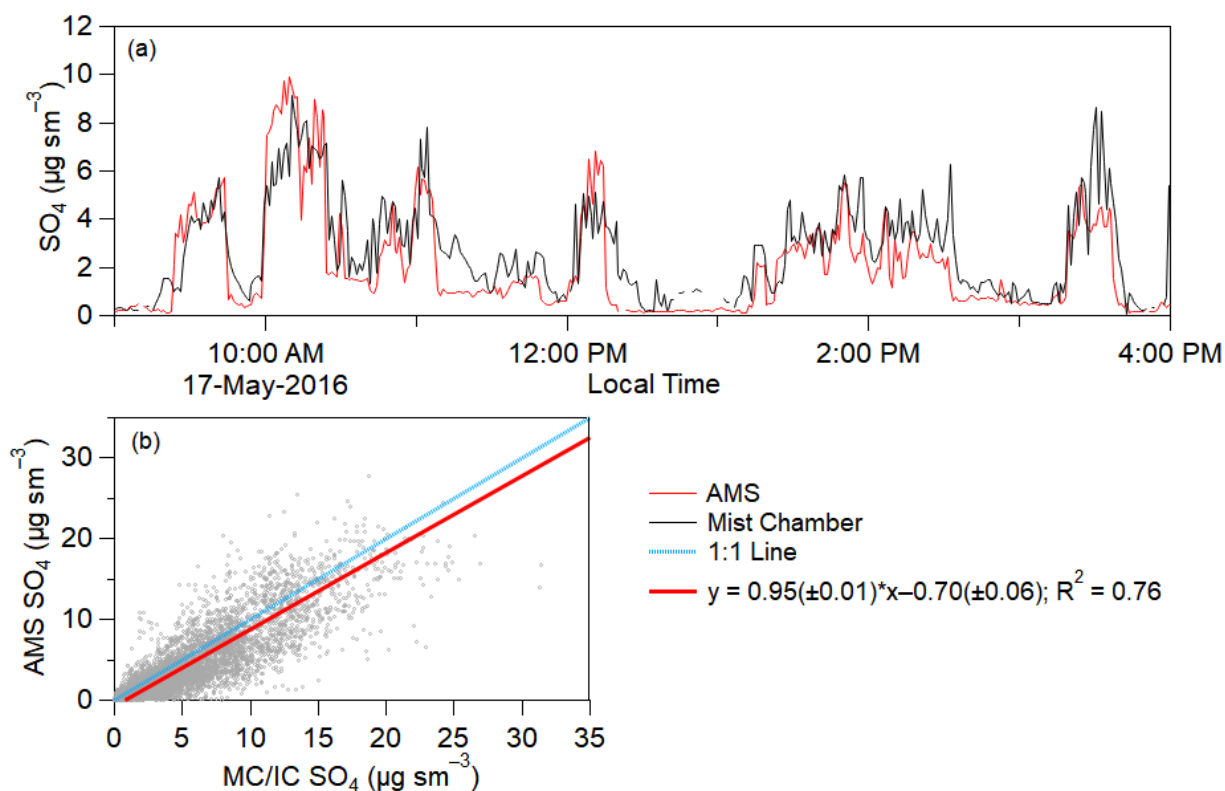


Figure S23. (top) Time series of mist-chamber (dark red line) and CU-AMS (red line) SO_4 for one flight (RF17). (bottom) Scatter plot of CU-AMS SO_4 versus mist-chamber ion-chromatograph (MC/IC) SO_4 for entire KORUS-AQ campaign.

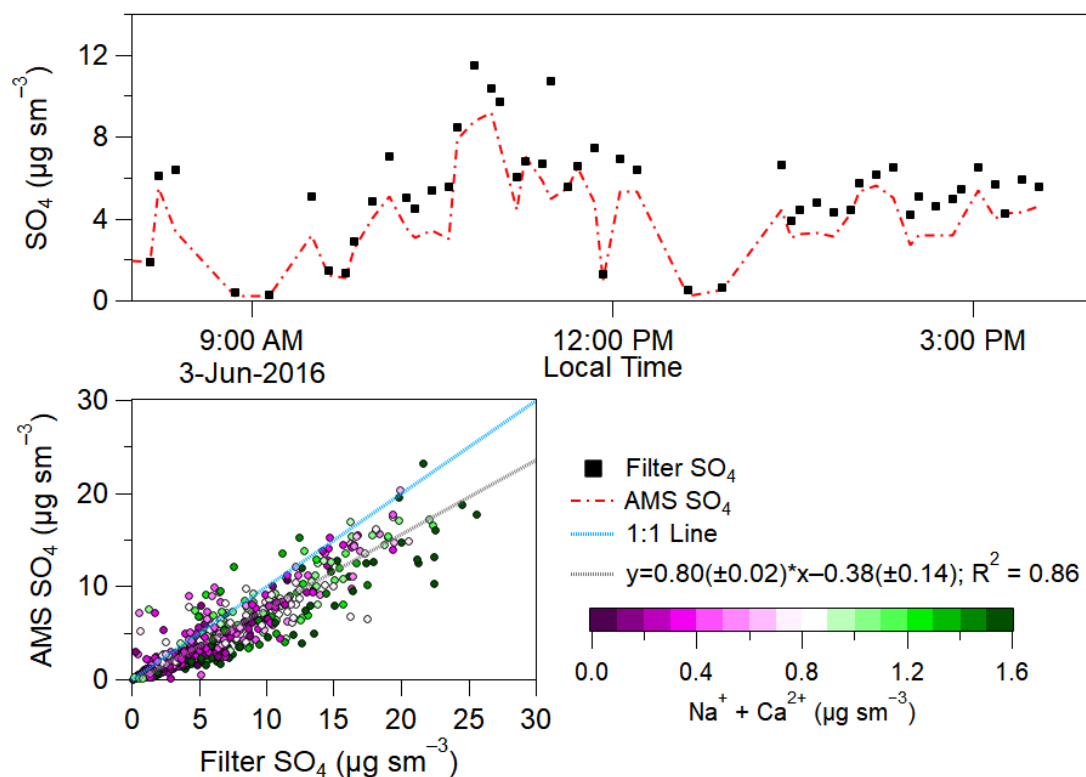


Figure S24. (top) Time series of filter (black squares) and CU-AMS (red line) SO_4 for one flight (RF17). The CU-AMS data has been averaged to the filter sampling time. (bottom) Scatter plot of CU-AMS SO_4 versus filter SO_4 for entire KORUS-AQ campaign. The points are colored by the total sodium (Na^+) and calcium (Ca^{2+}) measured by the filters, as indicators of sea salt and dust, respectively.

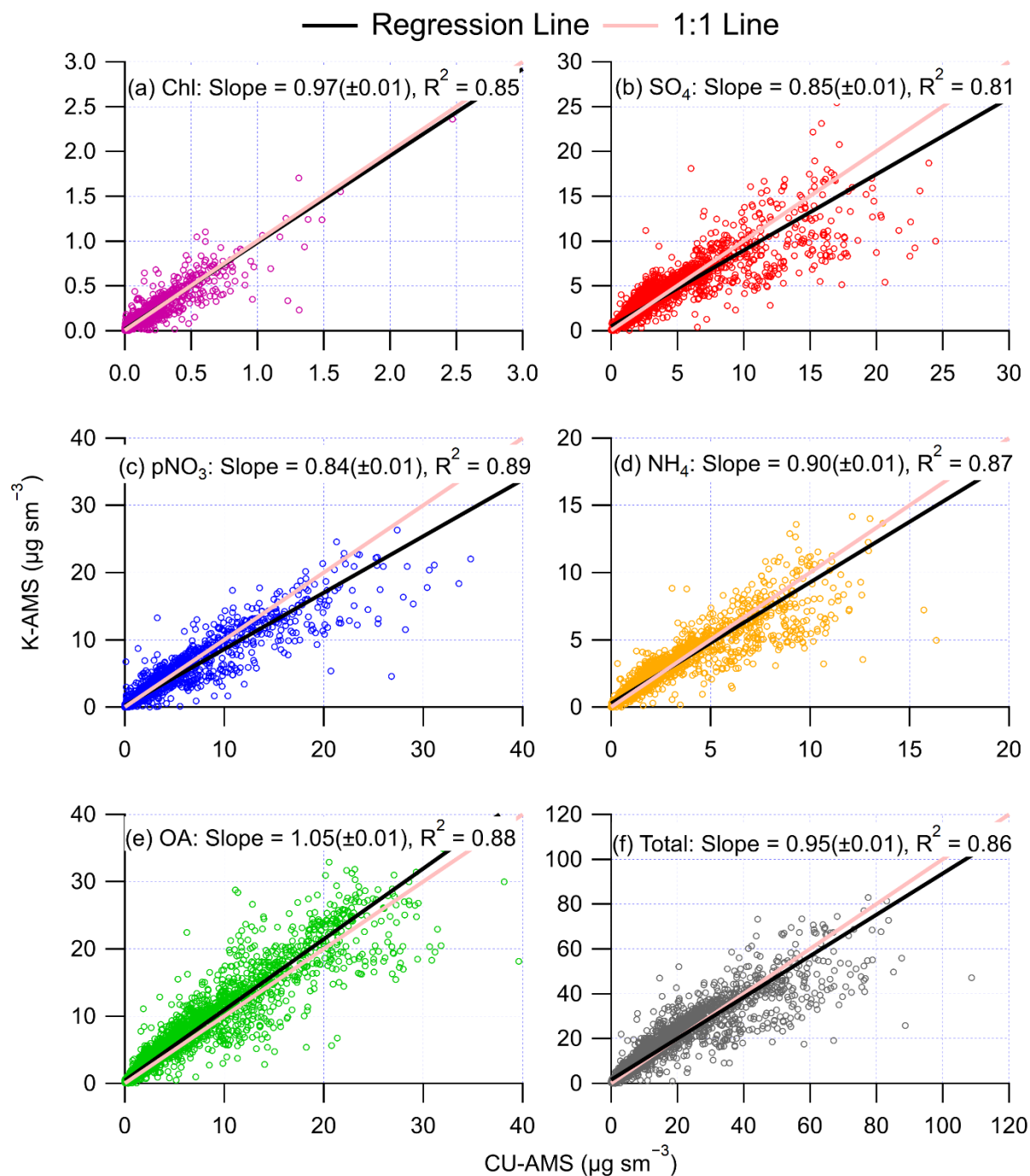


Figure S25. Scatter plot of not transmission corrected K-AMS versus CU-AMS mass concentrations for all of KORUS-AQ for (a) Chl, (b) SO_4 , (c) pNO_3 , (d) NH_4 , (e) OA, and (f) total AMS mass. The slopes and R^2 for all comparisons are shown in each scatter plot.

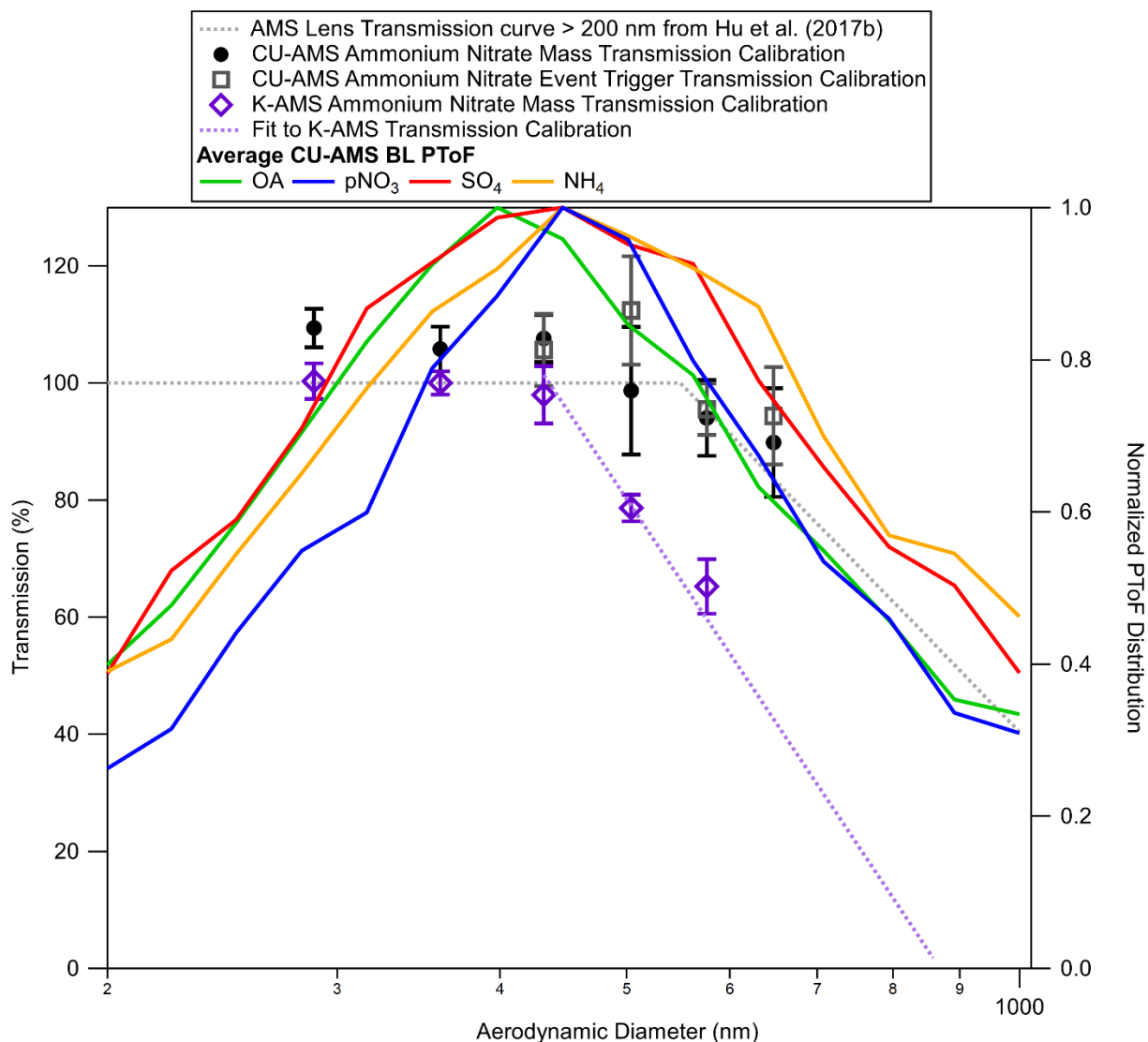


Figure S26. (left axis) Transmission curve for CU-AMS (black circle and dark grey square) and K-AMS (purple diamond). The curve from literature (Knote et al., 2011; Hu et al., 2017b), which describes the CU-AMS, is shown (grey dotted line). The fit for K-AMS transmission is shown with the purple dotted line. (right axis) Average mass distributions for OA (green), pNO₃ (blue), SO₄ (red), and NH₄ (orange) measured by CU-AMS in the boundary layer during KORUS-AQ. Note that some of the apparent signal at larger particle sizes is caused by the limited time response of the AMS detection system.

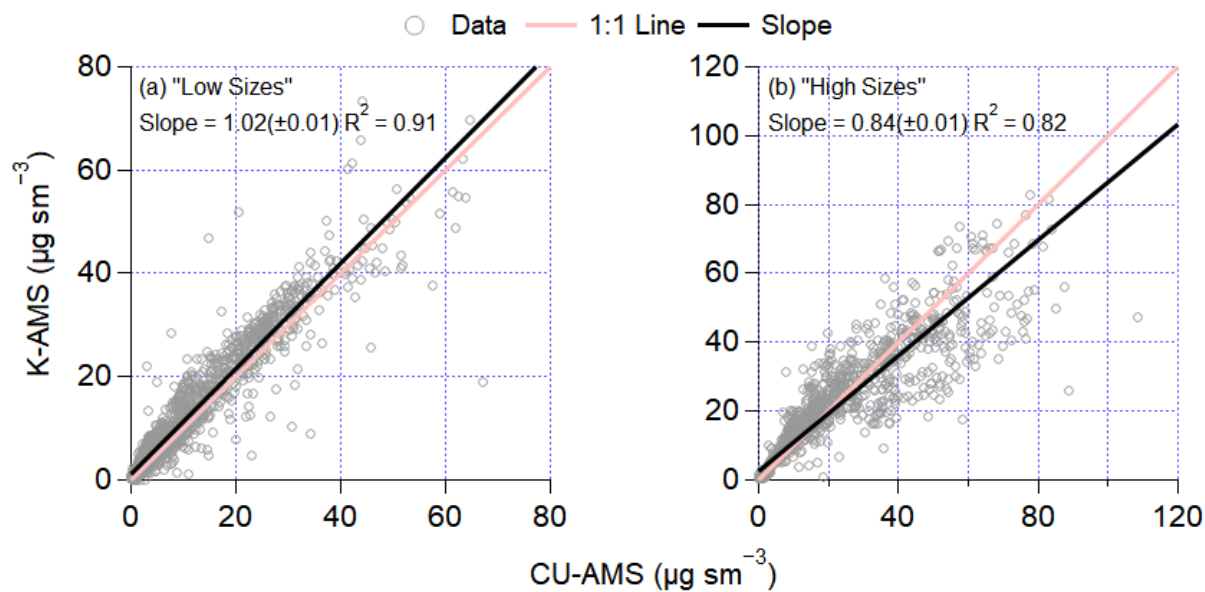


Figure S27. Scatter plot of K-AMS versus CU-AMS total mass concentrations (a) RFs 1 – 9, 11, 15, and 19 and (b) RFs 10, 12 – 14, 16 – 18, and 20. These are flights where the average sizes were found below (a) and above (b) the K-AMS size cut-off (Figure S26). The slopes and R^2 for all comparisons are shown in each scatter plot.

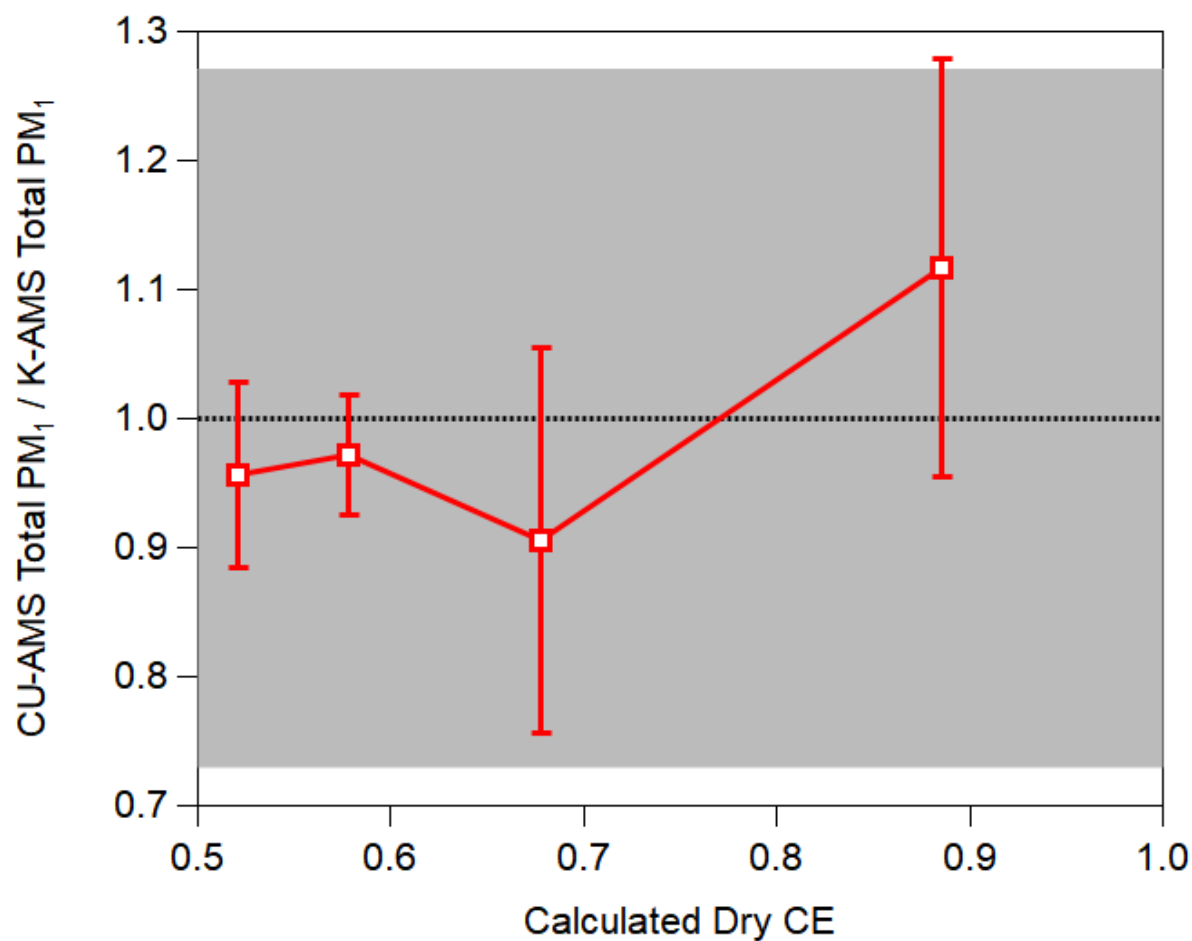


Figure S28. Binned total PM₁ AMS mass ratios, normalized by the average ratio, versus the calculated CE used for the CU-AMS measurements. The error bars are the standard error about the mean, and the shaded grey area is the combined uncertainty of the two AMS measurements ($\pm 27\%$). The data is only for flights where the PM₁ sizes were typically below the K-AMS size cut-off (RFs 1 – 9, 11, 15, and 19).

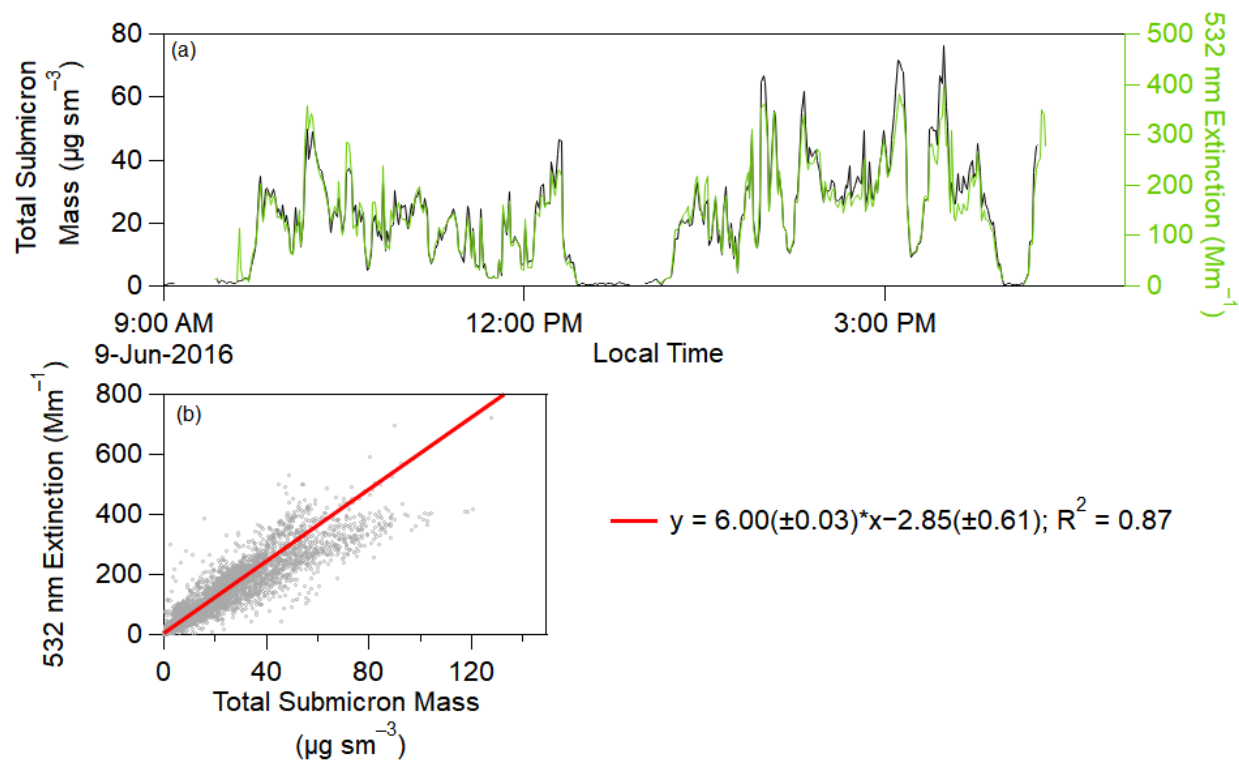


Figure S29. (top) Time series of total submicron mass (black, left axis) and 532 nm extinction (green, right axis) for one flight (RF19). (bottom) Scatter plot of 532 nm extinction versus total submicron mass (black carbon + CU-AMS species) for the entire KORUS-AQ campaign.

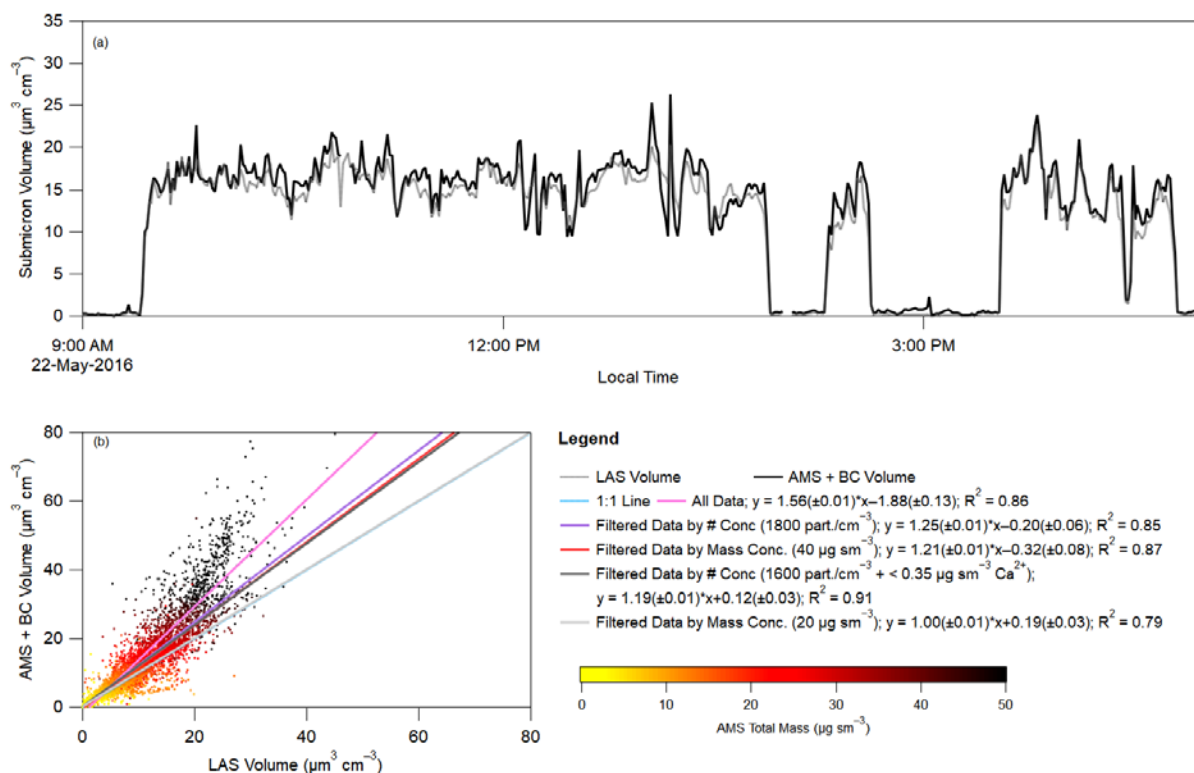


Figure S30. (top) Time series of total submicron volume from LAS (grey dashed line) and CU-AMS plus black carbon (black) for one flight (RF11). (bottom) Scatter plot of total submicron volume (black carbon + CU-AMS species) versus LAS volume for entire KORUS-AQ campaign. The data is colored by total CU-AMS mass. Pink line is a fit to all data, the purple line is a fit to data where the particle number concentration is less than $1800 \text{ particles cm}^{-3}$. The red line is a fit to the data where the CU-AMS plus SP2 total mass is less than $40 \mu\text{g sm}^{-3}$. The black line is a fit to the data where the particle number concentration is less than $1600 \text{ particles cm}^{-3}$ and Ca^{2+} concentration is less than $0.35 \mu\text{g sm}^{-3}$. Finally, the grey line is a fit to the data where the CU-AMS plus BC total mass is less than $20 \mu\text{g sm}^{-3}$.

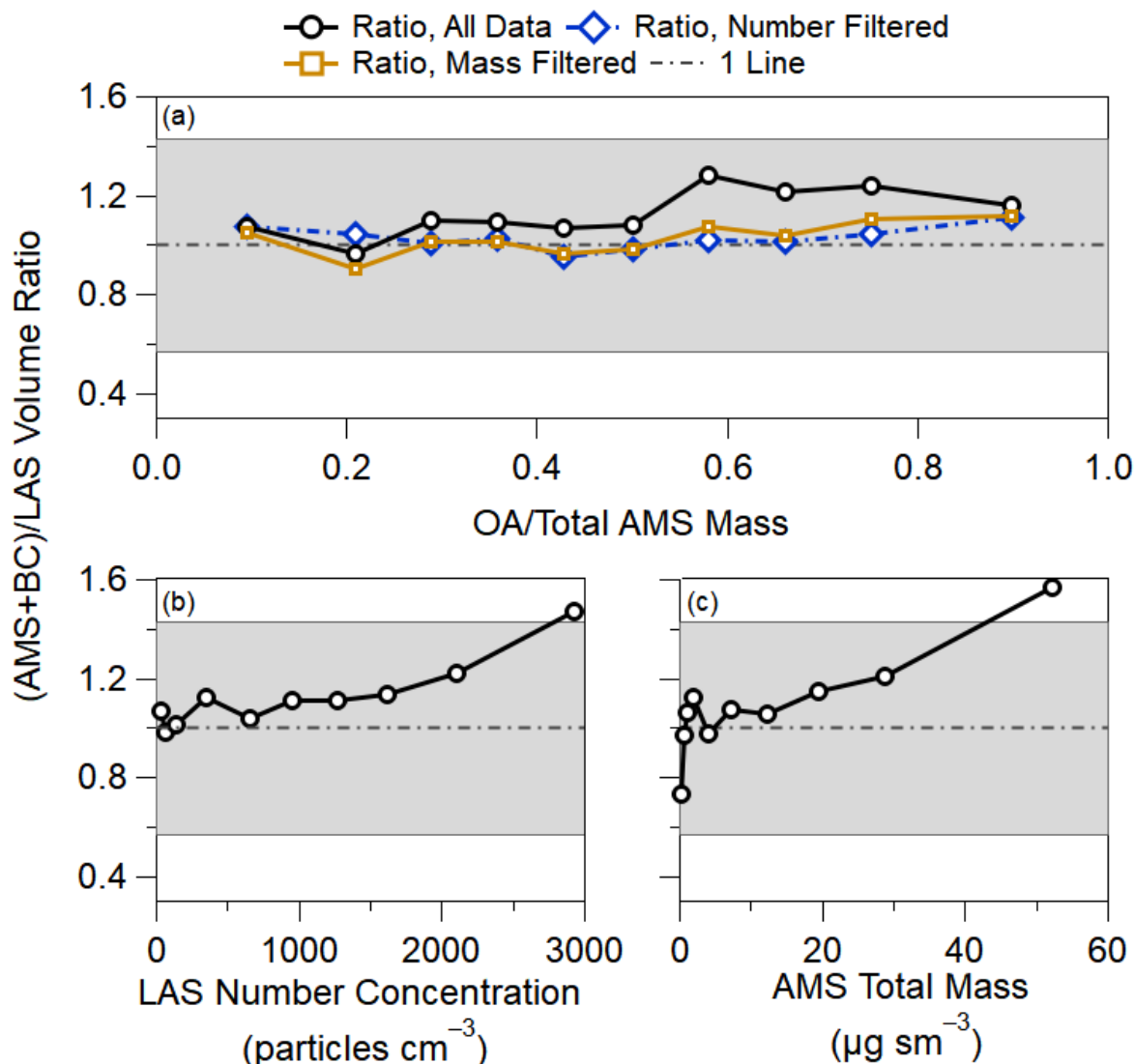
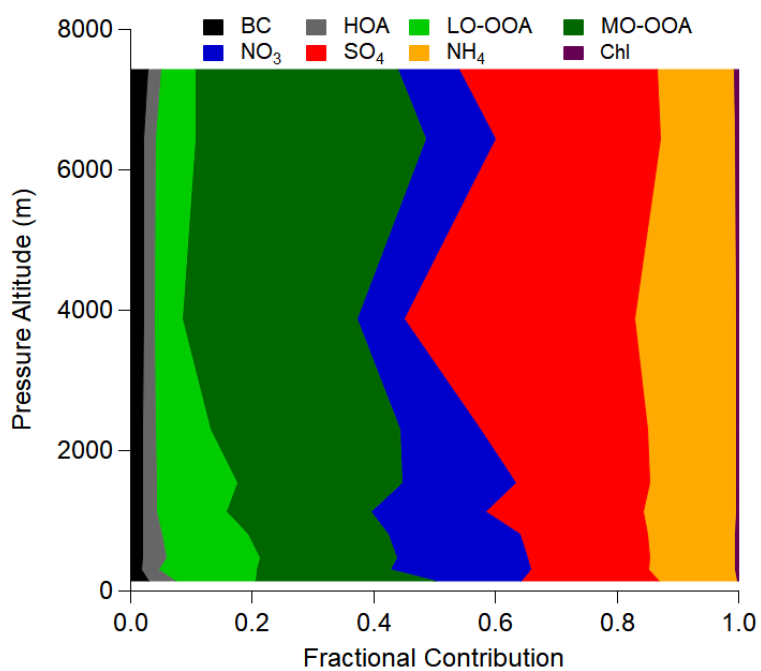


Figure S31. (a) Binned volume ratio (CU-AMS plus black carbon volume/LAS Volume) versus fraction of organic aerosol (OA) to total CU-AMS mass. (b) Binned volume ratio versus LAS particle number concentration. (c) Binned volume ratio versus CU-AMS total mass. In all figures, the black data is for all data whereas the blue data is for the volume ratio where the particle number concentration is less than 1600 particles cm⁻³ and the orange data is for the volume ratio where the CU-AMS total mass concentration is less than 20 μg sm⁻³. Also, the shaded area represents the combined uncertainty in both measurements (Bahreini et al., 2009).

529 **S9. Fractional PM₁ Contribution to Vertical Profile**



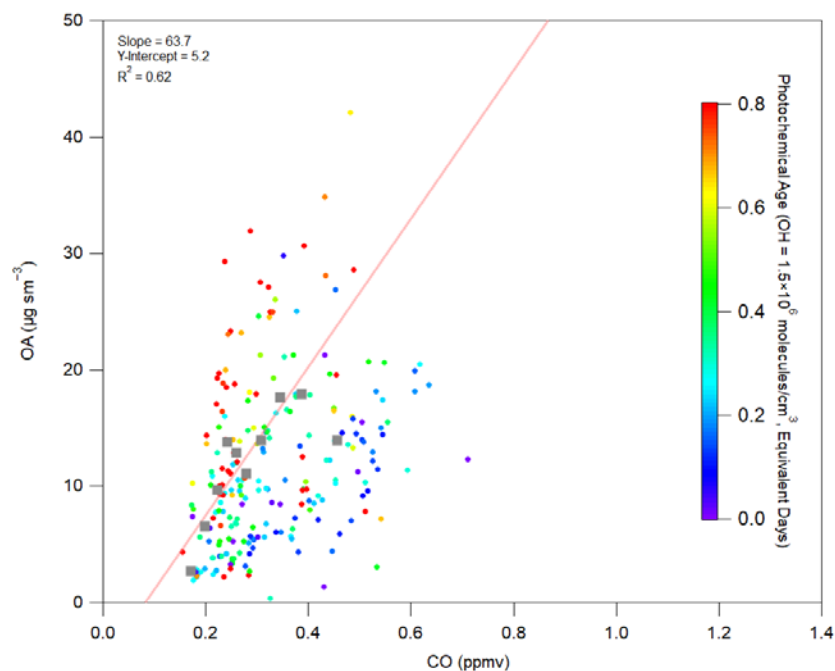
530

531 **Figure S32.** Fractional contribution of PM₁ contribution vertical profile for all of KORUS-AQ.

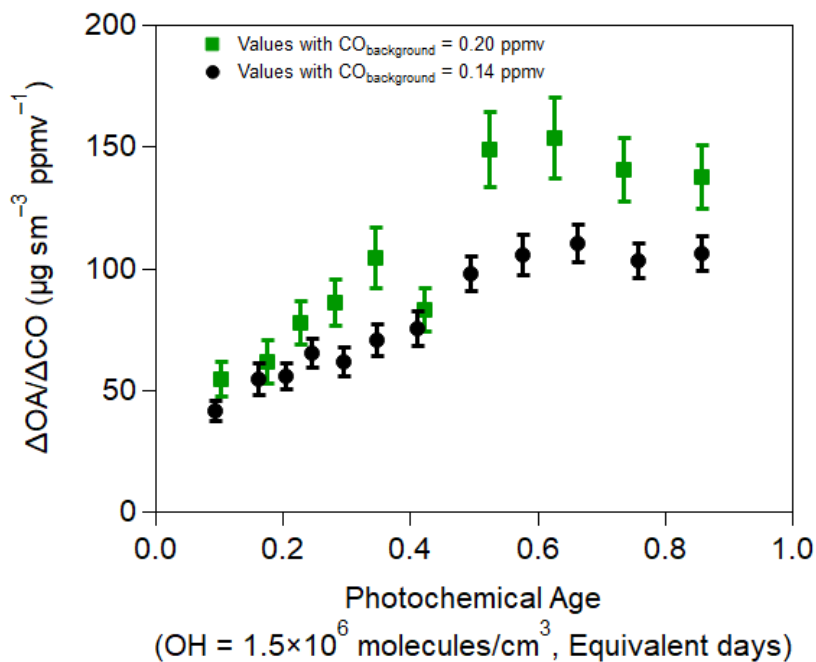
532

533

534 **S10. Observed Aerosol Production over Seoul, South Korea**



536 **Figure S33.** Scatter plot of OA versus CO, observed over Seoul, during KORUS-AQ. The points
537 are colored by the NO_x photochemical clock. The fit is for the decile binned data.



540 **Figure S34.** Comparison of $\Delta\text{OA}/\Delta\text{CO}$ observed over Seoul with different CO backgrounds.

Table S4. Compilation of slopes used to convert from $\Delta\text{OA}/\Delta\text{CO}$ to $\Delta\text{OA}/\Delta\text{CO}_2$ used in this study.

<i>Location</i>	<i>Slope (ppmv CO/ppmv CO₂)</i>	<i>Study</i>
Mexico City	0.045	Vay et al. (2009)
Los Angeles	0.009	Peischl et al., (2013)
Beijing	0.02	Wang et al. (2010)
		Silva et al. (2013)
		Tohjima et al. (2014)
Outflow China	0.02	Wang et al. (2010)
		Silva et al. (2013)
		Tohjima et al. (2014)
Seoul	0.01	Silva et al. (2013)
		Tang et al. (2018)

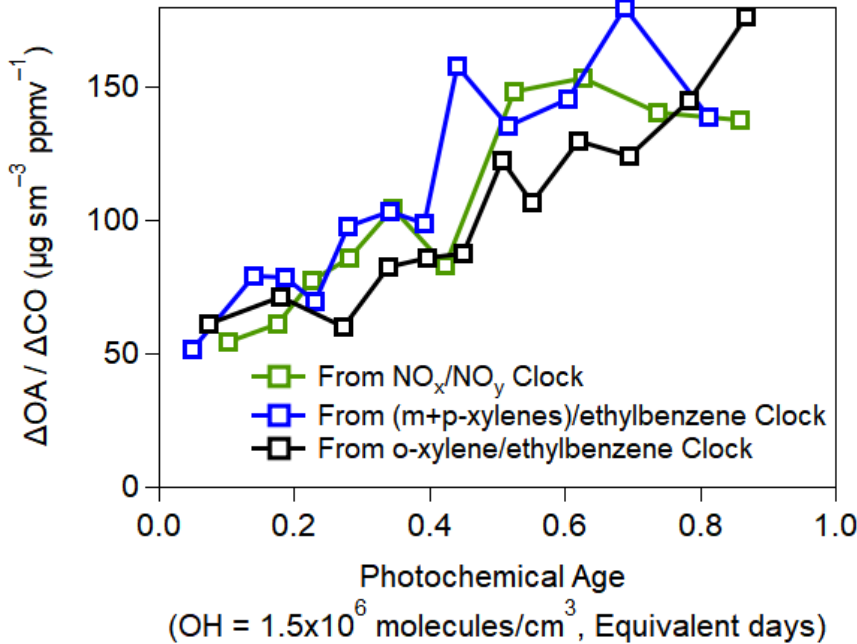
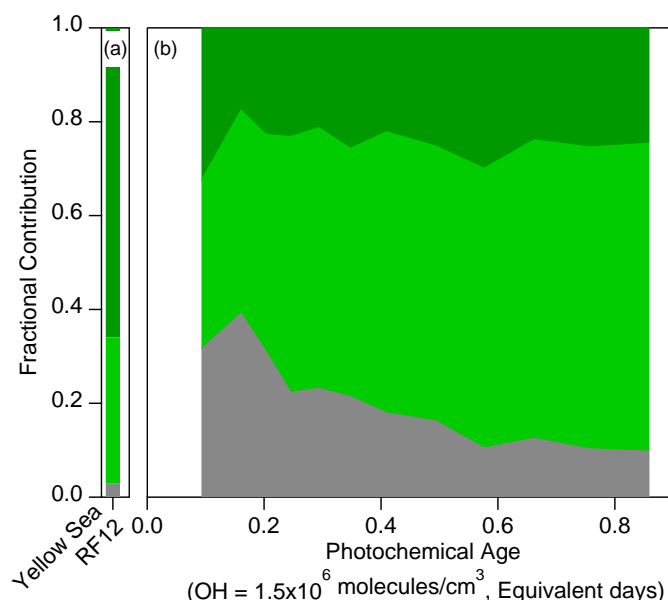


Figure S35. Same as **Figure 4(a)**, but comparing results using three different photochemical clocks (Figure S21).

548 S11. Oxidation of OA



549
 550 **Figure S36.** Same as **Figure 6b**, but speciated for MO-OOA, LO-OOA, and HOA. (a) is over the
 551 Yellow Sea (RF12) and (b) is over Seoul.

552 First, we briefly discuss how the AMS OA source tracers typically used to investigate OA
 553 chemistry evolved over Seoul (Figure S37). During KORUS-AQ, there was no appreciable
 554 influence from isoprene production of IEPOX-SOA (Hu et al., 2015), as the ion indicative of
 555 isoprene IEPOX-SOA ($C_5H_6O^+$) remained at background values typical of air without isoprene
 556 SOA influence.

557 Similarly, biomass burning OA (BBOA) appeared to be present but dilute in its
 558 contribution to OA. Most of the OA had $f_{C_2H_4O_2}$, an ion indicative of biomass burning and
 559 levoglucosan (Schneider et al., 2006; Aiken et al., 2010), below 0.1 over Seoul, and the PMF
 560 factors fall near the limit of detection for BBOA (Cubison et al., 2011) and lower than the values
 561 that typically indicate ambient and laboratory BBOA emissions at various stages of chemical
 562 evolution (Cubison et al., 2011; Ortega et al., 2013). We speculate that the limited BBOA is highly

563 mixed into the OA from the numerous, small agricultural fires that were observed during the
564 campaign and have been observed during this time period, during other years, in South Korea
565 (Kang et al., 2006). However, the amount of fresher BBOA was not high enough, nor as strong of
566 a feature as observed in prior studies (Aiken et al., 2010; DeCarlo et al., 2010; Cubison et al., 2011;
567 Hu et al., 2016), to reliably resolve a separate BBOA PMF factor. As shown in Figure S11, typical
568 gas-phase biomass burning tracers (CO, NO_x, acetonitrile, HCN, and black carbon) do not show a
569 consistent strong correlation with any of the PMF factors, further suggesting that BBOA is not a
570 major contributor, and any BBOA present is highly mixed with HOA and the oxidized OA.
571 Consistent with our results, Kim et al. (2017) did not resolve a BBOA factor from a ground site in
572 Seoul during the KORUS campaign.

573 Similar to other studies over urban areas or for chamber studies oxidizing urban VOCs
574 (e.g., benzene, xylenes, etc.) (Ng et al., 2010; Freney et al., 2014; Ortega et al., 2016), marked
575 chemical evolution was observed as tracked by the C₂H₃O⁺ and CO₂⁺ ions. The evolution of these
576 two ions, as a fraction of total OA, fall in the same space as has been observed in these prior
577 studies, indicating consistent photochemical evolution of SOA over urban locations.

578 Finally, unlike Kim et al. (2017), we did not observe clear indication for cooking organic
579 aerosol (COA) in our PMF results. The COA was at a minimum (less than 1 µg m⁻³) at the surface
580 in Seoul during the times the DC-8 overpassed (Kim et al., 2018); thus, we speculate the amount
581 of COA sampled was a small fraction of OA and was mostly lumped into the HOA factor. This
582 does not affect our characterization of HOA as POA, since COA is also a primary aerosol emission.

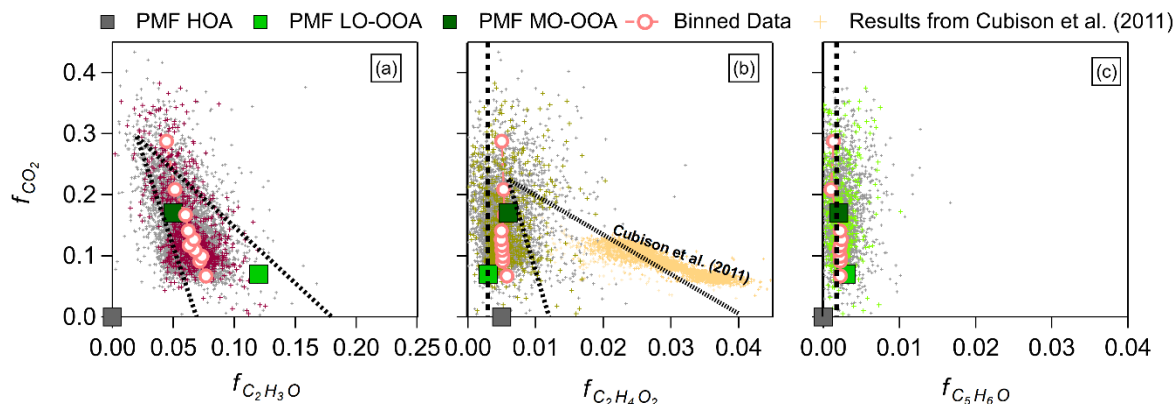
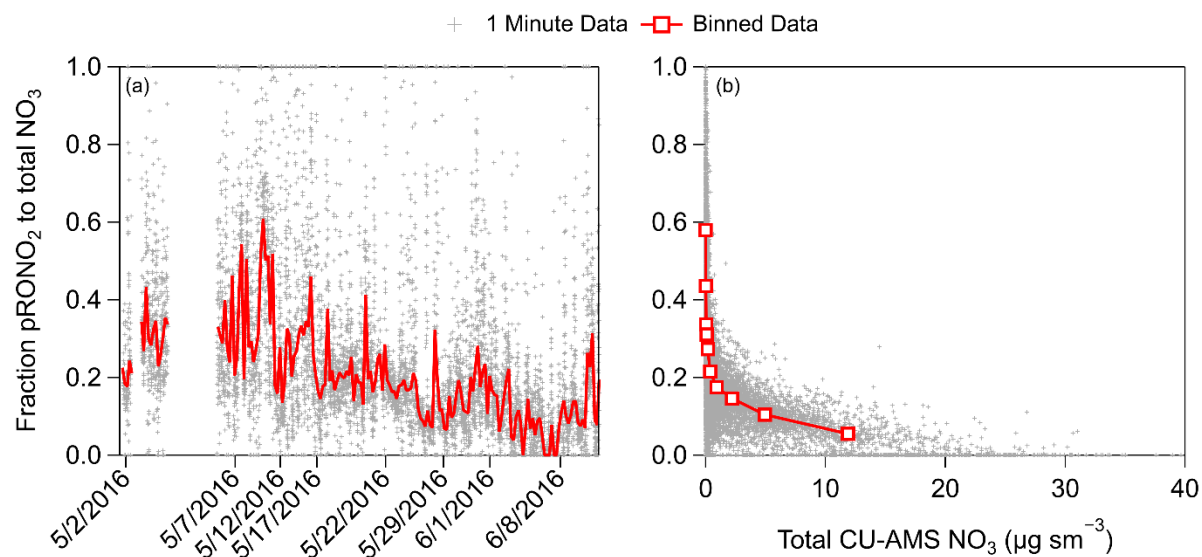


Figure S37. Plots of (a) f_{CO_2} versus $f_{C_2H_3O}$, (b) f_{CO_2} versus $f_{C_2H_4O_2}$, and (c) f_{CO_2} versus $f_{C_5H_6O}$. Points highlighted in color refer to observations over Seoul, South Korea, during KORUS-AQ. In (a), the triangle is from Ng et al. (2010); in (b), the triangle is from Cubison et al. (2011), and the vertical line is the typical “background” values for $f_{C_2H_4O_2}$ from Cubison et al. (2011); and, in (c), the vertical line is the typical “background” values for $f_{C_5H_6O}$ from Hu et al. (2015). The PMF results for each triangle plot are shown in squares, where grey is HOA, light green is LO-OOA, and dark green is MO-OOA. The light orange dots in (b) are the observations from ARCTAS forest fires (Cubison et al., 2011), as an example for data strongly impacted by biomass burning. The quantile average values (averaged the x variables according to quantiles of the y variables) for each comparison are shown in light red circles.

597 **S12. Particle organic nitrates**



598
 599 **Figure S38.** Time series of the fractional contribution of organic nitrates (pRONO₂) to the total
 600 pNO₃ signal during KORUS-AQ. (b) Fractional contribution of organic nitrates versus pNO₃
 601 during KORUS-AQ.

602

References

- Aiken, A. C., de Foy, B., Wiedinmyer, C., DeCarlo, P. F., Ulbrich, I. M., Wehrli, M. N., Szidat, S., Prévôt, A. S. H., Noda, J., Wacker, L., Volkamer, R., Fortner, E., Wang, J., Laskin, A., Shutthanandan, V., Zheng, J., Zhang, R., Paredes-Miranda, G., Arnott, W. P., Molina, L. T., Sosa, G., Querol, X. and Jimenez, J. L.: Mexico City aerosol analysis during MILAGRO using high resolution aerosol mass spectrometry at the urban supersite (T0)-Part 2: Analysis of the biomass burning contribution and the non-fossil carbon fraction, *Atmos. Chem. Phys.*, 10(12), 5315–5341, doi:10.5194/acp-10-5315-2010, 2010.
- Ait-Helal, W., Borbon, A., Sauvage, S., De Gouw, J. A., Colomb, A., Gros, V., Freutel, F., Crippa, M., Afif, C., Baltensperger, U., Beekmann, M., Doussin, J.-F. F., Durand-Jolibois, R., Fronval, I., Grand, N., Leonardis, T., Lopez, M., Michoud, V., Miet, K., Perrier, S., Prévôt, A. S. H., Schneider, J., Siour, G., Zapf, P. and Locoge, N.: Volatile and intermediate volatility organic compounds in suburban Paris: Variability, origin and importance for SOA formation, *Atmos. Chem. Phys.*, 14(19), 10439–10464, doi:10.5194/acp-14-10439-2014, 2014.
- Aknan, A. and Chen, G.: KORUS-AQ DC-8 Aircraft Dataset, [online] Available from: <https://www-air.larc.nasa.gov/cgi-bin/ArcView/korusaq> (Accessed 6 December 2018), 2018.
- Atkinson, R.: Kinetics of the gas-phase reactions of OH radicals with alkanes and cycloalkanes, *Atmos. Chem. Phys.*, 3(6), 2233–2307, doi:10.5194/acp-3-2233-2003, 2003.
- Atkinson, R. and Arey, J.: Atmospheric Degradation of Volatile Organic Compounds, *Chem. Rev.*, 103, 4605–4638, doi:10.1021/CR0206420, 2003.
- Atkinson, R., Baulch, D. L., Cox, R. A., Crowley, J. N., Hampson, R. F., Hynes, R. G., Jenkin, M. E., Rossi, M. J. and Troe, J.: Evaluated kinetic and photochemical data for atmospheric chemistry: Volume I - gas phase reactions of Ox, HO_x, NO_x and SO_x species, *Atmos. Chem. Phys.*, 4(6), 1461–1738, doi:10.5194/acp-4-1461-2004, 2004.
- Atkinson, R., Baulch, D. L., Cox, R. A., Crowley, J. N., Hampson, R. F., Hynes, R. G., Jenkin, M. E., Rossi, M. J., Troe, J. and IUPAC Subcommittee: Evaluated kinetic and photochemical data for atmospheric chemistry: Volume II - gas phase reactions of organic species, *Atmos. Chem. Phys.*, 6(11), 3625–4055, doi:10.5194/acp-6-3625-2006, 2006.
- Bahreini, R., Dunlea, E. J., Matthew, B. M., Simons, C., Docherty, K. S., DeCarlo, P. F., Jimenez, J. L., Brock, C. A. and Middlebrook, A. M.: Design and Operation of a Pressure-Controlled Inlet for Airborne Sampling with an Aerodynamic Aerosol Lens, *Aerosol Sci. Technol.*, 42(6), 465–471, doi:10.1080/02786820802178514, 2008.
- Bahreini, R., Ervens, B., Middlebrook, A. M., Warneke, C., de Gouw, J. A., DeCarlo, P. F., Jimenez, J. L., Brock, C. A., Neuman, J. A., Ryerson, T. B., Stark, H., Atlas, E., Brioude, J., Fried, A., Holloway, J. S., Peischl, J., Richter, D., Walega, J., Weibring, P., Wollny, A. G. and Fehsenfeld, F. C.: Organic aerosol formation in urban and industrial plumes near Houston and Dallas, Texas, *J. Geophys. Res.*, 114(16), D00F16, doi:10.1029/2008JD011493, 2009.
- Bohn, B. and Zetzsch, C.: Kinetics and mechanism of the reaction of OH with the trimethylbenzenes – experimental evidence for the formation of adduct isomers, *Phys. Chem. Chem. Phys.*, 14(40), 13933, doi:10.1039/c2cp42434g, 2012.
- Brioude, J., Arnold, D., Stohl, A., Cassiani, M., Morton, D., Seibert, P., Angevine, W., Evan, S.,

645 Dingwell, A., Fast, J. D., Easter, R. C., Pisso, I., Burkhardt, J. and Wotawa, G.: The Lagrangian
 646 particle dispersion model FLEXPART-WRF version 3.1, *Geosci. Model Dev.*, 6(6), 1889–1904,
 647 doi:10.5194/gmd-6-1889-2013, 2013.

648 Crounse, J. D., Nielsen, L. B., Jørgensen, S., Kjaergaard, H. G. and Wennberg, P. O.: Autoxidation
 649 of Organic Compounds in the Atmosphere, *J. Phys. Chem. Lett.*, 4(20), 3513–3520,
 650 doi:10.1021/jz4019207, 2013.

651 Cubison, M. J., Ortega, A. M., Hayes, P. L., Farmer, D. K., Day, D. A., Lechner, M. J., Brune, W.
 652 H., Apel, E., Diskin, G. S., Fisher, J. A., Fuelberg, H. E., Hecobian, A., Knapp, D. J., Mikoviny,
 653 T., Riemer, D., Sachse, G. W., Sessions, W., Weber, R. J., Weinheimer, A. J., Wisthaler, A. and
 654 Jimenez, J. L.: Effects of aging on organic aerosol from open biomass burning smoke in aircraft
 655 and laboratory studies, *Atmos. Chem. Phys.*, 11(23), 12049–12064, doi:10.5194/acp-11-12049-
 656 2011, 2011.

657 de Gouw, J. A., Gilman, J. B., Kim, S.-W., Lerner, B. M., Isaacman-VanWertz, G., McDonald, B.
 658 C., Warneke, C., Kuster, W. C., Lefer, B. L., Griffith, S. M., Dusanter, S., Stevens, P. S. and Stutz,
 659 J.: Chemistry of Volatile Organic Compounds in the Los Angeles basin: Nighttime Removal of
 660 Alkenes and Determination of Emission Ratios, *J. Geophys. Res.*, 122(21), 11,843–11,861,
 661 doi:10.1002/2017JD027459, 2017.

662 DeCarlo, P. F., Slowik, J. G., Worsnop, D. R., Davidovits, P., Jimenez, J. L., Stainken, K.,
 663 Williams, L., Jayne, J., Kolb, C. and Rudich, Y.: Particle Morphology and Density
 664 Characterization by Combined Mobility and Aerodynamic Diameter Measurements. Part 1:
 665 Theory, *Aerosol Sci. Technol.*, 38(12), 1185–1205, doi:10.1080/027868290903907, 2004.

666 DeCarlo, P. F., Dunlea, E. J., Kimmel, J. R., Aiken, A. C., Sueper, D., Crounse, J., Wennberg, P.
 667 O., Emmons, L., Shinozuka, Y., Clarke, A., Zhou, J., Tomlinson, J., Collins, D. R., Knapp, D.,
 668 Weinheimer, A. J., Montzka, D. D., Campos, T. and Jimenez, J. L.: Fast airborne aerosol size and
 669 chemistry measurements above Mexico City and Central Mexico during the MILAGRO campaign,
 670 *Atmos. Chem. Phys.*, 8(14), 4027–4048, doi:10.5194/acp-8-4027-2008, 2008.

671 DeCarlo, P. F., Ulbrich, I. M., Crounse, J., de Foy, B., Dunlea, E. J., Aiken, A. C., Knapp, D.,
 672 Weinheimer, A. J., Campos, T., Wennberg, P. O. and Jimenez, J. L.: Investigation of the sources
 673 and processing of organic aerosol over the Central Mexican Plateau from aircraft measurements
 674 during MILAGRO, *Atmos. Chem. Phys.*, 10(12), 5257–5280, doi:10.5194/acp-10-5257-2010,
 675 2010.

676 Docherty, K. S., Aiken, A. C., Huffman, J. A., Ulbrich, I. M., DeCarlo, P. F., Sueper, D., Worsnop,
 677 D. R., Snyder, D. C., Peltier, R. E., Weber, R. J., Grover, B. D., Eatough, D. J., Williams, B. J.,
 678 Goldstein, A. H., Ziemann, P. J. and Jimenez, J. L.: The 2005 Study of Organic Aerosols at
 679 Riverside (SOAR-1): instrumental intercomparisons and fine particle composition, *Atmos. Chem.*
 680 *Phys.*, 11(23), 12387–12420, doi:DOI 10.5194/acp-11-12387-2011, 2011.

681 Dunlea, E. J., DeCarlo, P. F., Aiken, A. C., Kimmel, J. R., Peltier, R. E., Weber, R. J., Tomlinson,
 682 J., Collins, D. R., Shinozuka, Y., McNaughton, C. S., Howell, S. G., Clarke, A. D., Emmons, L.
 683 K., Apel, E. C., Pfister, G. G., van Donkelaar, A., Martin, R. V., Millett, D. B., Heald, C. L. and
 684 Jimenez, J. L.: Evolution of Asian aerosols during transpacific transport in INTEX-B, *Atmos.*
 685 *Chem. Phys.*, 9(19), 7257–7287, doi:10.5194/acp-9-7257-2009, 2009.

686 Dzepina, K., Volkamer, R. M. R., Madronich, S., Tulet, P., Ulbrich, I. M., Zhang, Q., Cappa, C.
 687 D., Ziemann, P. J. and Jimenez, J. L.: Evaluation of recently-proposed secondary organic aerosol

models for a case study in Mexico City, *Atmos. Chem. Phys.*, 9(15), 5681–5709, doi:10.5194/acp-9-5681-2009, 2009.

Freney, E. J., Sellegri, K., Canonaco, F., Colomb, A., Borbon, A., Michoud, V., Doussin, J.-F., Crumeyrolle, S., Amarouche, N., Pichon, J.-M., Bourianne, T., Gomes, L., Prevot, A. S. H., Beekmann, M. and Schwarzenböck, A.: Characterizing the impact of urban emissions on regional aerosol particles: airborne measurements during the MEGAPOLI experiment, *Atmos. Chem. Phys.*, 14(3), 1397–1412, doi:10.5194/acp-14-1397-2014, 2014.

Fry, J. L., Draper, D. C., Zarzana, K. J., Campuzano-Jost, P., Day, D. A., Jimenez, J. L., Brown, S. S., Cohen, R. C., Kaser, L., Hansel, A., Cappellin, L., Karl, T., Hodzic Roux, A., Turnipseed, A., Cantrell, C., Lefer, B. L. and Grossberg, N.: Observations of gas- and aerosol-phase organic nitrates at BEACHON-RoMBAS 2011, *Atmos. Chem. Phys.*, 13(17), 8585–8605, doi:10.5194/acp-13-8585-2013, 2013.

Hand, J. L. and Malm, W. C.: Review of aerosol mass scattering efficiencies from ground-based measurements since 1990, *J. Geophys. Res.*, 112(D16), D16203, doi:10.1029/2007JD008484, 2007.

Hayes, P. L., Ortega, A. M., Cubison, M. J., Froyd, K. D., Zhao, Y., Cliff, S. S., Hu, W. W., Toohey, D. W., Flynn, J. H., Lefer, B. L., Grossberg, N., Alvarez, S., Rappenglück, B., Taylor, J. W., Allan, J. D., Holloway, J. S., Gilman, J. B., Kuster, W. C., de Gouw, J. A., Massoli, P., Zhang, X., Liu, J., Weber, R. J., Corrigan, A. L., Russell, L. M., Isaacman, G., Worton, D. R., Kreisberg, N. M., Goldstein, A. H., Thalman, R., Waxman, E. M., Volkamer, R., Lin, Y. H., Surratt, J. D., Kleindienst, T. E., Offenberg, J. H., Dusanter, S., Griffith, S., Stevens, P. S., Brioude, J., Angevine, W. M. and Jimenez, J. L.: Organic aerosol composition and sources in Pasadena, California, during the 2010 CalNex campaign, *J. Geophys. Res.*, 118(16), 9233–9257, doi:10.1002/jgrd.50530, 2013.

Heim, E., Dibb, J., Scheuer, E., Campuzano-Jost, P., Nault, B. A., Jimenez, J. L., Peterson, D., Knote, C., Fenn, M., Hair, J., Beyersdorf, A. J. and Anderson, B. E.: Asian Dust Observed during KORUS-AQ Facilitates the Uptake and Incorporation of Soluble Pollutants during Transport to South Korea: The Hwangsa Anthropogenic Model, *J. Geophys. Res. Atmos.*, submitted, 2018.

Heo, J.-B., Hopke, P. K. and Yi, S.-M.: Source apportionment of PM_{2.5} in Seoul, Korea, *Atmos. Chem. Phys.*, 9(14), 4957–4971, doi:10.5194/acp-9-4957-2009, 2009.

Hu, W., Hu, M., Hu, W., Jimenez, J. L., Yuan, B., Chen, W., Wang, M., Wu, Y., Chen, C., Wang, Z., Peng, J., Zeng, L. and Shao, M.: Chemical composition, sources and aging process of sub-micron aerosols in Beijing: contrast between summer and winter, *J. Geophys. Res. Atmos.*, doi:10.1002/2015JD024020, 2016.

Hu, W., Campuzano-Jost, P., Day, D. A., Croteau, P., Canagaratna, M. R., Jayne, J. T., Worsnop, D. R. and Jimenez, J. L.: Evaluation of the new capture vaporizer for aerosol mass spectrometers (AMS) through field studies of inorganic species, *Aerosol Sci. Technol.*, 51(6), 735–754, doi:10.1080/02786826.2017.1296104, 2017a.

Hu, W., Campuzano-Jost, P., Day, D. A., Croteau, P., Canagaratna, M. R., Jayne, J. T., Worsnop, D. R. and Jimenez, J. L.: Evaluation of the new capture vapourizer for aerosol mass spectrometers (AMS) through laboratory studies of inorganic species, *Atmos. Meas. Tech.*, 10(6), 2897–2921, doi:10.5194/amt-10-2897-2017, 2017b.

Hu, W., Day, D. A., Campuzano-Jost, P., Nault, B. A., Park, T., Lee, T., Croteau, P., Canagaratna,

730 M. R., Jayne, J. T., Worsnop, D. R. and Jimenez, J. L.: Evaluation of the new capture vaporizer
 731 for Aerosol Mass Spectrometers: Characterization of organic aerosol mass spectra, *Aerosol Sci.*
 732 *Technol.*, 52(7), 752–739, doi:10.1080/02786826.2018.1454584, 2018a.

733 Hu, W., Day, D. A., Campuzano-Jost, P., Nault, B. A., Park, T., Lee, T., Croteau, P., Canagaratna,
 734 M. R., Jayne, J. T., Worsnop, D. R. and Jimenez, J. L.: Evaluation of the New Capture Vaporizer
 735 for Aerosol Mass Spectrometers (AMS): Elemental Composition and Source Apportionment of
 736 Organic Aerosols (OA), *ACS Earth Sp. Chem.*, 2(4), 410–421,
 737 doi:10.1021/acsearthspacechem.8b00002, 2018b.

738 Hu, W. W., Campuzano-Jost, P., Palm, B. B., Day, D. A., Ortega, A. M., Hayes, P. L., Krechmer,
 739 J. E., Chen, Q., Kuwata, M., Liu, Y. J., de Sá, S. S., McKinney, K., Martin, S. T., Hu, M.,
 740 Budisulistiorini, S. H., Riva, M., Surratt, J. D., St. Clair, J. M., Isaacman-Van Wertz, G., Yee, L.
 741 D., Goldstein, A. H., Carbone, S., Brito, J., Artaxo, P., de Gouw, J. A., Koss, A., Wisthaler, A.,
 742 Mikoviny, T., Karl, T., Kaser, L., Jud, W., Hansel, A., Docherty, K. S., Alexander, M. L.,
 743 Robinson, N. H., Coe, H., Allan, J. D., Canagaratna, M. R., Paulot, F. and Jimenez, J. L.:
 744 Characterization of a real-time tracer for Isoprene Epoxydiols-derived Secondary Organic Aerosol
 745 (IEPOX-SOA) from aerosol mass spectrometer measurements, *Atmos. Chem. Phys.*, 15(8),
 746 11807–11833, doi:10.5194/acp-15-11807-2015, 2015.

747 Huffman, J. A., Docherty, K. S., Aiken, A. C., Cubison, M. J., Ulbrich, I. M., DeCarlo, P. F.,
 748 Sueper, D., Jayne, J. T., Worsnop, D. R., Ziemann, P. J. and Jimenez, J. L.: Chemically-resolved
 749 aerosol volatility measurements from two megacity field studies, *Atmos. Chem. Phys.*, 9(1), 7161–
 750 7182, doi:doi:10.5194/acp-9-7161-2009, 2009.

751 Jimenez, J. L., Canagaratna, M. R., Donahue, N. M., Prevot, A. S. H., Zhang, Q., Kroll, J. H.,
 752 DeCarlo, P. F., Allan, J. D., Coe, H., Ng, N. L., Aiken, A. C., Docherty, K. S., Ulbrich, I. M.,
 753 Grieshop, A. P., Robinson, A. L., Duplissy, J., Smith, J. D., Wilson, K. R., Lanz, V. A., Hueglin,
 754 C., Sun, Y. L., Tian, J., Laaksonen, A., Raatikainen, T., Rautiainen, J., Vaattovaara, P., Ehn, M.,
 755 Kulmala, M., Tomlinson, J. M., Collins, D. R., Cubison, M. J., Dunlea, E. J., Huffman, J. A.,
 756 Onasch, T. B., Alfarra, M. R., Williams, P. I., Bower, K., Kondo, Y., Schneider, J., Drewnick, F.,
 757 Borrmann, S., Weimer, S., Demerjian, K., Salcedo, D., Cottrell, L., Griffin, R., Takami, A.,
 758 Miyoshi, T., Hatakeyama, S., Shimono, A., Sun, J. Y., Zhang, Y. M., Dzepina, K., Kimmel, J. R.,
 759 Sueper, D., Jayne, J. T., Herndon, S. C., Trimborn, A. M., Williams, L. R., Wood, E. C.,
 760 Middlebrook, A. M., Kolb, C. E., Baltensperger, U., Worsnop, D. R. and Worsnop, D. R.:
 761 Evolution of organic aerosols in the atmosphere., *Science*, 326(5959), 1525–1529,
 762 doi:10.1126/science.1180353, 2009.

763 Jimenez, J. L., Canagaratna, M. R., Drewnick, F., Allan, J. D., Alfarra, M. R., Middlebrook, A.
 764 M., Slowik, J. G., Zhang, Q., Coe, H., Jayne, J. T. and Worsnop, D. R.: Comment on “The effects
 765 of molecular weight and thermal decomposition on the sensitivity of a thermal desorption aerosol
 766 mass spectrometer,” *Aerosol Sci. Technol.*, 50(9), i–xv, doi:10.1080/02786826.2016.1205728,
 767 2016.

768 Kang, C. M., Kang, B. W. and Lee, H. S.: Source identification and trends in concentrations of
 769 gaseous and fine particulate principal species in Seoul, South Korea, *J. Air Waste Manag. Assoc.*,
 770 56(7), 911–921, doi:10.1080/10473289.2006.10464506, 2006.

771 Kim, B. M., Seo, J., Kim, J. Y., Lee, J. Y. and Kim, Y.: Transported vs. local contributions from
 772 secondary and biomass burning sources to PM_{2.5}, *Atmos. Environ.*, 144, 24–36,

doi:10.1016/j.atmosenv.2016.08.072, 2016.

Kim, H., Zhang, Q. and Heo, J.: Influence of Intense secondary aerosol formation and long-range transport on aerosol chemistry and properties in the Seoul Metropolitan Area during spring time : Results from KORUS-AQ, *Atmos. Chem. Phys.*, 18, 7149–7168, doi:10.5194/acp-2017-947, 2018.

Kleinman, L. I., Springston, S. R., Daum, P. H., Lee, Y.-N., Nunnermacker, L. J., Senum, G. I., Wang, J., Weinstein-Lloyd, J., Alexander, M. L., Hubbe, J., Ortega, J., Canagaratna, M. R. and Jayne, J.: The time evolution of aerosol composition over the Mexico City plateau, *Atmos. Chem. Phys.*, 8(6), 1559–1575, doi:10.5194/acp-8-1559-2008, 2008.

Knote, C., Brunner, D., Vogel, H., Allan, J., Asmi, A., Äijälä, M., Carbone, S., van der Gon, H. D., Jimenez, J. L., Kiendler-Scharr, A., Mohr, C., Poulain, L., Prévôt, A. S. H., Swietlicki, E. and Vogel, B.: Towards an online-coupled chemistry-climate model: evaluation of trace gases and aerosols in COSMO-ART, *Geosci. Model Dev.*, 4(4), 1077–1102, doi:10.5194/gmd-4-1077-2011, 2011.

Krechmer, J. E., Pagonis, D., Ziemann, P. J. and Jimenez, J. L.: Quantification of Gas-Wall Partitioning in Teflon Environmental Chambers Using Rapid Bursts of Low-Volatility Oxidized Species Generated in Situ, *Environ. Sci. Technol.*, 50(11), 5757–5765, doi:10.1021/acs.est.6b00606, 2016.

Kuwata, M., Zorn, S. R. and Martin, S. T.: Using Elemental Ratios to Predict the Density of Organic Material Composed of Carbon, Hydrogen, and Oxygen, *Environ. Sci. Technol.*, 46(2), 787–794, doi:10.1021/es202525q, 2012.

Lide, D. R.: *CRC Handbook of Chemistry and Physics*, CRC Press Inc., USA., 1991.

Liu, P. S. K., Deng, R., Smith, K. A., Williams, L. R., Jayne, J. T., Canagaratna, M. R., Moore, K., Onasch, T. B., Worsnop, D. R. and Deshler, T.: Transmission Efficiency of an Aerodynamic Focusing Lens System: Comparison of Model Calculations and Laboratory Measurements for the Aerodyne Aerosol Mass Spectrometer, *Aerosol Sci. Technol.*, 41(8), 721–733, doi:10.1080/02786820701422278, 2007.

Liu, X., Huey, L. G., Yokelson, R. J., Selimovic, V., Simpson, I. J., Müller, M., Jimenez, J. L., Campuzano-Jost, P., Beyersdorf, A. J., Blake, D. R., Butterfield, Z., Choi, Y., Crounse, J. D., Day, D. A., Diskin, G. S., Dubey, M. K., Fortner, E., Hanisco, T. F., Hu, W., King, L. E., Kleinman, L., Meinardi, S., Mikoviny, T., Onasch, T. B., Palm, B. B., Peischl, J., Pollack, I. B., Ryerson, T. B., Sachse, G. W., Sedlacek, A. J., Shilling, J. E., Springston, S., St. Clair, J. M., Tanner, D. J., Teng, A. P., Wennberg, P. O., Wisthaler, A. and Wolfe, G. M.: Airborne measurements of western U.S. wildfire emissions: Comparison with prescribed burning and air quality implications, *J. Geophys. Res.*, 122(11), 6108–6129, doi:10.1002/2016JD026315, 2017.

Ma, P. K., Zhao, Y., Robinson, A. L., Worton, D. R., Goldstein, A. H., Ortega, A. M., Jimenez, J.-L., Zotter, P., Prévôt, A. S. H., Szidat, S. and Hayes, P. L.: Evaluating the impact of new observational constraints on P-S/IVOC emissions, multi-generation oxidation, and chamber wall losses on SOA modeling for Los Angeles, CA, *Atmos. Chem. Phys.*, 17(15), 9237–9259, doi:10.5194/acp-17-9237-2017, 2017.

McNaughton, C. S., Clarke, A. D., Howell, S. G., Pinkerton, M., Anderson, B., Thornhill, L., Hudgins, C., Winstead, E., Dibb, J. E., Scheuer, E. and Maring, H.: Results from the DC-8 Inlet

815 Characterization Experiment (DICE): Airborne versus surface sampling of mineral dust and sea
816 salt aerosols, *Aerosol Sci. Technol.*, 41(2), 136–159, doi:10.1080/02786820601118406, 2007.

817 Middlebrook, A. M., Bahreini, R., Jimenez, J. L. and Canagaratna, M. R.: Evaluation of
818 Composition-Dependent Collection Efficiencies for the Aerodyne Aerosol Mass Spectrometer
819 using Field Data, *Aerosol Sci. Technol.*, 46(3), 258–271, doi:10.1080/02786826.2011.620041,
820 2012.

821 Moise, T., Flores, J. M. and Rudich, Y.: Optical Properties of Secondary Organic Aerosols and
822 Their Changes by Chemical Processes, *Chem. Rev.*, 115(10), 4400–4439, doi:10.1021/cr5005259,
823 2015.

824 Mollner, A. K., Valluvadasan, S., Feng, L., Sprague, M. K., Okumura, M., Milligan, D. B., Bloss,
825 W. J., Sander, S. P., Martien, P. T., Harley, R. a, McCoy, A. B. and Carter, W. P. L.: Rate of Gas
826 Phase Association of Hydroxyl Radical and Nitrogen Dioxide, *Science* (80-.), 330(6004), 646–
827 9, doi:10.1126/science.1193030, 2010.

828 Murphy, D. M.: The effects of molecular weight and thermal decomposition on the sensitivity of
829 a thermal desorption aerosol mass spectrometer, *Aerosol Sci. Technol.*, 50(2), 118–125,
830 doi:10.1080/02786826.2015.1136403, 2016.

831 Nault, B. A., Campuzano-Jost, P., Schroder, J. C., Sueper, D. and Jimenez, J. L.: Using Event
832 Trigger Panel for IE/AB and Transmission Curve Calibrations, in 17th AMS Users' Meeting,
833 Portland. [online] Available from: [http://cires1.colorado.edu/jimenez-](http://cires1.colorado.edu/jimenez-group/wiki/index.php/AMSUrMtg#17th_AMS_Users_Meeting.2C_Portland.2C_Oregon)
834 [group/wiki/index.php/AMSUrMtg#17th_AMS_Users_Meeting.2C_Portland.2C_Oregon](http://cires1.colorado.edu/jimenez-group/wiki/index.php/AMSUrMtg#17th_AMS_Users_Meeting.2C_Portland.2C_Oregon),
835 2016.

836 NCEP: National Centers for Environmental Prediction, [online] Available from:
837 <http://www.emc.ncep.noaa.gov/GFS/doc.php> (Accessed 16 November 2017), n.d.

838 Neuman, J. A., Parrish, D. D., Ryerson, T. B., Brock, C. A., Wiedinmyer, C., Frost, G. J.,
839 Holloway, J. S. and Fehsenfeld, F. C.: Nitric acid loss rates measured in power plant plumes, *J.*
840 *Geophys. Res.*, 109(23), 1–13, doi:10.1029/2004JD005092, 2004.

841 Ng, N. L., Canagaratna, M. R., Zhang, Q., Jimenez, J. L., Tian, J., Ulbrich, I. M., Kroll, J. H.,
842 Docherty, K. S., Chhabra, P. S., Bahreini, R., Murphy, S. M., Seinfeld, J. H., Hildebrandt, L.,
843 Donahue, N. M., Decarlo, P. F., Lanz, V. A., Prévôt, A. S. H., Dinar, E., Rudich, Y. and Worsnop,
844 D. R.: Organic aerosol components observed in Northern Hemispheric datasets from Aerosol Mass
845 Spectrometry, *Atmos. Chem. Phys.*, 10(10), 4625–4641, doi:10.5194/acp-10-4625-2010, 2010.

846 Nguyen, T. B., Crounse, J. D., Teng, A. P., St. Clair, J. M., Paulot, F., Wolfe, G. M. and Wennberg,
847 P. O.: Rapid deposition of oxidized biogenic compounds to a temperate forest, *Proc. Natl. Acad.*
848 *Sci.*, 112(5), E392–E401, doi:10.1073/pnas.1418702112, 2015.

849 Ortega, A. M., Day, D. A., Cubison, M. J., Brune, W. H., Bon, D., de Gouw, J. A. and Jimenez, J.
850 L.: Secondary organic aerosol formation and primary organic aerosol oxidation from biomass-
851 burning smoke in a flow reactor during FLAME-3, *Atmos. Chem. Phys.*, 13(22), 11551–11571,
852 doi:10.5194/acp-13-11551-2013, 2013.

853 Ortega, A. M., Hayes, P. L., Peng, Z., Palm, B. B., Hu, W., Day, D. A., Li, R., Cubison, M. J.,
854 Brune, W. H., Graus, M., Warneke, C., Gilman, J. B., Kuster, W. C., de Gouw, J. A., Gutiérrez-
855 Montes, C. and Jimenez, J. L.: Real-time measurements of secondary organic aerosol formation
856 and aging from ambient air in an oxidation flow reactor in the Los Angeles area, *Atmos. Chem.*

857 Phys., 16(11), 7411–7433, doi:10.5194/acp-16-7411-2016, 2016.

858 Palm, B. B., Campuzano-Jost, P., Ortega, A. M., Day, D. A., Kaser, L., Jud, W., Karl, T., Hansel,
859 A., Hunter, J. F., Cross, E. S., Kroll, J. H., Peng, Z., Brune, W. H. and Jimenez, J. L.: In situ
860 secondary organic aerosol formation from ambient pine forest air using an oxidation flow reactor,
861 Atmos. Chem. Phys., 16(5), 2943–2970, doi:10.5194/acp-16-2943-2016, 2016.

862 Palm, B. B., Campuzano-Jost, P., Day, D. A., Ortega, A. M., Fry, J. L., Brown, S. S., Zarzana, K.
863 J., Dube, W., Wagner, N. L., Draper, D. C., Kaser, L., Jud, W., Karl, T., Hansel, A., Gutiérrez-
864 Montes, C. and Jimenez, J. L.: Secondary organic aerosol formation from in situ OH, O₃, and NO₃
865 oxidation of ambient forest air in an oxidation flow reactor, Atmos. Chem. Phys., 17(8), 5331–
866 5354, doi:10.5194/acp-17-5331-2017, 2017.

867 Palm, B. B., de Sá, S. S., Day, D. A., Campuzano-Jost, P., Hu, W., Seco, R., Sjostedt, S. J., Park,
868 J.-H., Guenther, A. B., Kim, S., Brito, J., Wurm, F., Artaxo, P., Thalman, R., Wang, J., Yee, L. D.,
869 Wernis, R., Isaacman-VanWertz, G., Goldstein, A. H., Liu, Y., Springston, S. R., Souza, R.,
870 Newburn, M. K., Alexander, M. L., Martin, S. T. and Jimenez, J. L.: Secondary organic aerosol
871 formation from ambient air in an oxidation flow reactor in central Amazonia, Atmos. Chem. Phys.,
872 18(1), 467–493, doi:10.5194/acp-18-467-2018, 2018.

873 Park, K., Kittelson, D. B., Zachariah, M. R. and McMurry, P. H.: Measurement of Inherent
874 Material Density of Nanoparticle Agglomerates, J. Nanoparticle Res., 6(2/3), 267–272,
875 doi:10.1023/B:NANO.0000034657.71309.e6, 2004.

876 Parrish, D. D., Stohl, A., Forster, C., Atlas, E. L., Blake, D. R., Goldan, P. D., Kuster, W. C. and
877 de Gouw, J. A.: Effects of mixing on evolution of hydrocarbon ratios in the troposphere, J.
878 Geophys. Res., 112(D10), D10S34, doi:10.1029/2006JD007583, 2007.

879 Peischl, J., Ryerson, T. B., Brioude, J., Aikin, K. C., Andrews, A. E., Atlas, E., Blake, D., Daube,
880 B. C., de Gouw, J. A., Dlugokencky, E., Frost, G. J., Gentner, D. R., Gilman, J. B., Goldstein, A.
881 H., Harley, R. A., Holloway, J. S., Kofler, J., Kuster, W. C., Lang, P. M., Novelli, P. C., Santoni,
882 G. W., Trainer, M., Wofsy, S. C. and Parrish, D. D.: Quantifying sources of methane using light
883 alkanes in the Los Angeles basin, California, J. Geophys. Res. Atmos., 118(10), 4974–4990,
884 doi:10.1002/jgrd.50413, 2013.

885 Peng, Z., Day, D. A., Stark, H., Li, R., Lee-Taylor, J., Palm, B. B., Brune, W. H. and Jimenez, J.
886 L.: HO_x radical chemistry in oxidation flow reactors with low-pressure mercury lamps
887 systematically examined by modeling, Atmos. Meas. Tech., 8(11), 4863–4890, doi:10.5194/amt-
888 8-4863-2015, 2015.

889 Pieber, S. M., El Haddad, I., Slowik, J. G., Canagaratna, M. R., Jayne, J. T., Platt, S. M., Bozzetti,
890 C., Daellenbach, K. R., Fröhlich, R., Vlachou, A., Klein, F., Dommen, J., Miljevic, B., Jiménez,
891 J. L., Worsnop, D. R., Baltensperger, U. and Prévôt, A. S. H.: Inorganic Salt Interference on CO₂+
892 in Aerodyne AMS and ACSM Organic Aerosol Composition Studies, Environ. Sci. Technol.,
893 50(19), 10494–10503, doi:10.1021/acs.est.6b01035, 2016.

894 Robinson, A. L., Donahue, N. M., Shrivastava, M. K., Weitkamp, E. A., Sage, A. M., Grieshop,
895 A. P., Lane, T. E., Pierce, J. R. and Pandis, S. N.: Rethinking Organic Aerosols: Semivolatile
896 Emissions and Photochemical Aging, Science (80-.), 315(5816), 1259–1262,
897 doi:10.1126/science.1133061, 2007.

898 Romer, P. S., Duffey, K. C., Wooldridge, P. J., Allen, H. M., Ayres, B. R., Brown, S. S., Brune,

899 W. H., Crounse, J. D., de Gouw, J., Draper, D. C., Feiner, P. A., Fry, J. L., Goldstein, A. H., Koss,
900 A., Misztal, P. K., Nguyen, T. B., Olson, K., Teng, A. P., Wennberg, P. O., Wild, R. J., Zhang, L.
901 and Cohen, R. C.: The lifetime of nitrogen oxides in an isoprene-dominated forest, *Atmos. Chem.*
902 *Phys.*, 16(12), 7623–7637, doi:10.5194/acp-16-7623-2016, 2016.

903 Salcedo, D., Onasch, T. B., Dzepina, K., Canagaratna, M. R., Zhang, Q., Huffman, J. A., Decarlo,
904 P. F., Jayne, J. T., Mortimer, P., Worsnop, D. R., Kolb, C. E., Johnson, K. S., Zuberi, B., Marr, L.
905 C., Volkamer, R., Molina, L. T., Molina, M. J., Cardenas, B., Bernabe, R. M., Marquez, C.,
906 Gaffney, J. S., Marley, N. A., Laskin, A., Shutthanandan, V., Xie, Y., Brune, W., Leshner, R.,
907 Shirley, T. and Jimenez, J. L.: Characterization of ambient aerosols in Mexico City during the
908 MCMA-2003 campaign with Aerosol Mass Spectrometry: results from the CENICA Supersite,
909 *Atmos. Chem. Phys.*, 6(4), 925–946, doi:10.5194/acp-6-925-2006, 2006.

910 Sander, S. P., Abbatt, J. P. D., Barker, J. R., Burkholder, J. B., Friedl, R. R., Golden, D. M., Huie,
911 R. E., Kolb, C. E., Kurylo, M. J., Moortgat, G. K., Orkin, V. L. and Wine, P. H.: Chemical Kinetics
912 and Photochemical Data for Use in Atmospheric Studies, Evaluation No. 17, JPL Publ. 10-6, Jet
913 Propuls. Lab. Pasadena, 2011.

914 Schneider, J., Hings, S. S., Nele Hock, B., Weimer, S., Borrmann, S., Fiebig, M., Petzold, A.,
915 Busen, R. and Kärcher, B.: Aircraft-based operation of an aerosol mass spectrometer:
916 Measurements of tropospheric aerosol composition, *J. Aerosol Sci.*, 37(7), 839–857,
917 doi:10.1016/j.jaerosci.2005.07.002, 2006.

918 Shinozuka, Y., Clarke, A. D., DeCarlo, P. F., Jimenez, J. L., Dunlea, E. J., Roberts, G. C.,
919 Tomlinson, J. M., Collins, D. R., Howell, S. G., Kapustin, V. N., McNaughton, C. S. and Zhou, J.:
920 Aerosol optical properties relevant to regional remote sensing of CCN activity and links to their
921 organic mass fraction: airborne observations over Central Mexico and the US West Coast during
922 MILAGRO/INTEX-B, *Atmos. Chem. Phys.*, 9(18), 6727–6742, 2009.

923 Silva, S. J., Arellano, A. F. and Worden, H. M.: Toward anthropogenic combustion emission
924 constraints from space-based analysis of urban CO₂/CO sensitivity, *Geophys. Res. Lett.*, 40(18),
925 4971–4976, doi:10.1002/grl.50954, 2013.

926 Skamarock, C., Klemp, B., Dudhia, J., Gill, O., Barker, D., Duda, G., Huang, X., Wang, W. and
927 Powers, G.: A Description of the Advanced Research WRF Version 3, , doi:10.5065/D68S4MVH,
928 2008.

929 Sprengnether, M. M., Demerjian, K. L., Dransfield, T. J., Clarke, J. S., Anderson, J. G. and
930 Donahue, N. M.: Rate Constants of Nine C₆-C₉ Alkanes with OH from 230 to 379 K: Chemical
931 Tracers for [OH], *J. Phys. Chem. A*, 113, 5030–5038, doi:10.1021/jp810412m, 2009.

932 TAbMET: TAbMEP Assessment: POLARCAT HNO₃ Summary, in TAbMEP
933 POLARCAT/ICARTT Analysis, edited by G. Chen, [https://www-](https://www-air.larc.nasa.gov/TAbMEP2_polarcat.html)
934 [air.larc.nasa.gov/TAbMEP2_polarcat.html](https://www-air.larc.nasa.gov/TAbMEP2_polarcat.html), Boulder., 2009.

935 Tang, W., Arellano, A. F., DiGangi, J. P., Choi, Y., Diskin, G. S., Agustí-Panareda, A., Parrington,
936 M., Massart, S., Gaubert, B., Lee, Y., Kim, D., Jung, J., Hong, J., Hong, J.-W., Kanaya, Y., Lee,
937 M., Stauffer, R. M., Thompson, A. M., Flynn, J. H. and Woo, J.-H.: Evaluating High-Resolution
938 Forecasts of Atmospheric CO and CO₂ from a Global Prediction System during KORUS-AQ Field
939 Campaign, *Atmos. Chem. Phys. Discuss.*, 1–41, doi:10.5194/acp-2018-71, 2018.

940 Thornton, J. A., Wooldridge, P. J., Cohen, R. C., Martinez, M., Harder, H., Brune, W. H.,

941 Williams, E. J. J., Roberts, J. M. M., Fehsenfeld, F. C., Hall, S. R., Shetter, R. E. E., Wert, B. P.
 942 and Fried, A.: Ozone production rates as a function of NO_x abundances and HO_x production rates
 943 in the Nashville urban plume, *J. Geophys. Res.*, 107(D12), 1–17, doi:10.1029/2001JD000932,
 944 2002.

945 Tohjima, Y., Kubo, M., Minejima, C., Mukai, H., Tanimoto, H., Ganshin, A., Maksyutov, S.,
 946 Katsumata, K., Machida, T. and Kita, K.: Temporal changes in the emissions of CH₄ and CO from
 947 China estimated from CH₄ / CO₂ and CO / CO₂ correlations observed at Hateruma Island, *Atmos.*
 948 *Chem. Phys.*, 14(3), 1663–1677, doi:10.5194/acp-14-1663-2014, 2014.

949 Ulbrich, I. M., Canagaratna, M. R., Zhang, Q., Worsnop, D. R. and Jimenez, J. L.: Interpretation
 950 of organic components from Positive Matrix Factorization of aerosol mass spectrometric data,
 951 *Atmos. Chem. Phys.*, 9(9), 2891–2918, doi:10.5194/acp-9-2891-2009, 2009.

952 Vay, S. A., Tyler, S. C., Choi, Y., Blake, D. R., Blake, N. J., Sachse, G. W., Diskin, G. S. and
 953 Singh, H. B.: Sources and transport of $\Delta^{14}\text{C}$ in CO₂ within the Mexico City Basin and vicinity,
 954 *Atmos. Chem. Phys.*, 9, 4973–4985, doi:10.5194/acp-9-4973-2009, 2009.

955 Wang, Y., Munger, J. W., Xu, S., McElroy, M. B., Hao, J., Nielsen, C. P. and Ma, H.: CO₂ and its
 956 correlation with CO at a rural site near Beijing: implications for combustion efficiency in China,
 957 *Atmos. Chem. Phys.*, 10(18), 8881–8897, doi:10.5194/acp-10-8881-2010, 2010.

958 Williams, L.: What is My Vaporizer Temperature? Vaporizer Temperature Power Curve for
 959 Several Systems, [online] Available from: [http://cires1.colorado.edu/jimenez-](http://cires1.colorado.edu/jimenez-group/UsrMtgs/UsersMtg11/WilliamsAMSUsersMtg_2010_VapT.pdf)
 960 [group/UsrMtgs/UsersMtg11/WilliamsAMSUsersMtg_2010_VapT.pdf](http://cires1.colorado.edu/jimenez-group/UsrMtgs/UsersMtg11/WilliamsAMSUsersMtg_2010_VapT.pdf) (Accessed 12 March
 961 2018), 2010.

962 Woo, J.-H., An, S.-M., Kim, D.-Y., Kim, H.-K., Choi, K.-C. and Kim, Y.-H.: Development of the
 963 Asia Emission Inventory in Support of Integrated Modeling of Climate and Air Quality (III),
 964 Incheon, Korea., 2013.

965 Xu, W., Croteau, P., Williams, L., Canagaratna, M., Onasch, T., Cross, E., Zhang, X., Robinson,
 966 W., Worsnop, D. and Jayne, J.: Laboratory characterization of an aerosol chemical speciation
 967 monitor with PM_{2.5} measurement capability, *Aerosol Sci. Technol.*, 51(1), 69–83,
 968 doi:10.1080/02786826.2016.1241859, 2017.

969 Xu, W., Lambe, A., Silva, P., Hu, W., Onasch, T., Williams, L., Croteau, P., Zhang, X., Renbaum-
 970 Wolff, L., Fortner, E., Jimenez, J. L., Jayne, J., Worsnop, D. and Canagaratna, M.: Laboratory
 971 evaluation of species-dependent relative ionization efficiencies in the Aerodyne Aerosol Mass
 972 Spectrometer, *Aerosol Sci. Technol.*, 1–16, doi:10.1080/02786826.2018.1439570, 2018.

973 Yuan, B., Hu, W. W., Shao, M., Wang, M., Chen, W. T., Lu, S. H., Zeng, L. M. and Hu, M.: VOC
 974 emissions, evolutions and contributions to SOA formation at a receptor site in eastern China,
 975 *Atmos. Chem. Phys.*, 13(17), 8815–8832, doi:10.5194/acp-13-8815-2013, 2013.

976 Zhang, Q., Stanier, C. O., Canagaratna, M. R., Jayne, J. T., Worsnop, D. R., Pandis, S. N. and
 977 Jimenez, J. L.: Insights into the chemistry of new particle formation and growth events in
 978 Pittsburgh based on aerosol mass spectrometry, *Environ. Sci. Technol.*, 38(18), 4797–4809,
 979 doi:10.1021/Es035417u, 2004.

980 Zhang, Q., Alfarra, M. R., Worsnop, D. R., James, D., Coe, H., Canagaratna, M. R. and Jimenez,
 981 J. L.: Deconvolution and Quantification of Hydrocarbon-like and Oxygenated Organic Aerosols
 982 Based on Aerosol Mass Spectrometry Deconvolution and Quantification of Hydrocarbon-like and

983 Oxygenated Organic Aerosols Based on Aerosol Mass Spectrometry, *Environ. Sci. Technol.*,
984 39(13), 4938–4952, doi:10.1021/es048568l, 2005.

985 Zhao, Y., Hennigan, C. J., May, A. A., Tkacik, D. S., de Gouw, J. A., Gilman, J. B., Kuster, W.
986 C., Borbon, A. and Robinson, A. L.: Intermediate-volatility organic compounds: a large source of
987 secondary organic aerosol, *Environ. Sci. Technol.*, 48(23), 13743–50, doi:10.1021/es5035188,
988 2014.

989

990